TALLINN UNIVERSITY OF TECHNOLOGY

SCHOOL OF ENGINEERING

Department of materials and environmental technology

EFFECT OF TiO_2 ANNEALING CONDITIONS ON THE PERFORMANCE OF ANTIMONY SELENIDE THIN FILM SOLAR CELL

TiO_2 kilede lõõmutamise mõju õhukesekilelise antimonseleniidi päikesepatarei tõhususele

MASTER THESIS

Student: Mykhailo Koltsov

Student code: 194266KAYM

Supervisors:

Dr. Nicolae Spalatu

Dr. Atanas Katerski

Tallinn 2021

(On the reverse side of title page)

AUTHOR'S DECLARATION

Hereby I declare, that I have written this thesis independently.
No academic degree has been applied for based on this material. All works, major viewpoints, and data of the other authors used in this thesis have been referenced.

"....." May 2021

Author: Mykhailo Koltsov

/signature/

Thesis is in accordance with terms and requirements

"....." May 2021

Supervisor: Dr. Nicolae Spalatu

/signature/

Accepted for defence

"....." May 2021

Chairman of theses defence commission: .....

/name and signature/

Non-exclusive licence for reproduction and publication of a graduation thesis[1]

I, Mykhailo Koltsov,

1. grant Tallinn University of Technology free licence (non-exclusive licence) for my thesis "Effect of TiO2 annealing conditions on the performance of antimony selenide thin film solar cell",

supervised by Dr. Nicolae Spalatu and Dr. Atanas Katerski,

1.1 to be reproduced for the purposes of preservation and electronic publication of the graduation thesis, incl. to be entered in the digital collection of the library of Tallinn University of Technology until expiry of the term of copyright;

1.2 to be published via the web of Tallinn University of Technology, incl. to be entered in the digital collection of the library of Tallinn University of Technology until expiry of the term of copyright.

2. I am aware that the author also retains the rights specified in clause 1 of the non-exclusive licence.

3. I confirm that granting the non-exclusive licence does not infringe other persons' intellectual property rights, the rights arising from the Personal Data Protection Act or rights arising from other legislation.

21.05.2021

[1] *The non-exclusive licence is not valid during the validity of access restriction indicated in the student's application for restriction on access to the graduation thesis that has been signed by the school's dean, except in case of the university's right to reproduce the thesis for preservation purposes only. If a graduation thesis is based on the joint creative activity of two or more persons and the co-author(s) has/have not granted, by the set deadline, the student defending his/her graduation thesis consent to reproduce and publish the graduation thesis in compliance with clauses 1.1 and 1.2 of the non-exclusive licence, the non-exclusive license shall not be valid for the period.*

Faculty of Chemical and Materials Technology

THESIS TASK

Student: Mykhailo Koltsov, 194266KAYM

Study programme, main specialty: KAYM Materials and Processes for Sustainable Energetics materials for sustainable energetics

Supervisor(s): Research Scientist, Dr. Nicolae Spalatu, +3726203366
Research Scientist, Dr. Atanas Katerski, +3726203369

Thesis topic:

(in English) EFFECT OF TIO_2 ANNEALING CONDITIONS ON THE PERFORMANCE OF ANTIMONY SELENIDE THIN FILM SOLAR CELL

(in Estonian) TiO_2 kilede lõõmutamise mõju õhukesekilelise antimonseleniidi päikesepatarei tõhususele

Thesis main objectives:

1. To learn about the working principles of thin film solar cells, thin film deposition methods and characterization techniques for thin film / thin film solar cell analysis.
2. To familiarize with the USP and CSS deposition techniques for TiO_2 and Sb_2Se_3 respectively.
3. To analyze the influence of the annealing temperature and environment onto structural and exploitation properties of TiO_2/Sb_2Se_3 thin film solar cells.

No	Task description	Deadline
1.	USP-deposition of the first set of samples (TiO_2/FTO/Glass), material characterization of the samples (XRD, UV-VIS)	
2.	USP- and CSS-deposition of the second set of samples (glass/FTO/TiO_2/ Sb_2Se_3/Au), material characterization of the samples (XRD)	
3	Solar cell performance evaluation (J-V, EQE) for samples from second set, XPS analysis	
4.	Analysis of acquired data and last thesis preparations	

Language: English **Deadline for submission of thesis:** 21rd May 2021.

Student: Mykhailo Koltsov ..... May 2021

/signature/

Supervisor: Dr. Nicolae Spalatu ..... May 2021

/signature/

Co-supervisor: Dr. Atanas Katerski ..... May 2021

/signature/

Head of study programme: Professor Sergei Bereznev ..... May 2021

/signature/

Contents

PREFACE

Dr. Nicolae Spalatu proposed the concept of the following thesis, and the dominant part of the work was carried out in the Laboratory of Thin Film Chemical Technologies. My biggest thanks go to my supervisors, Dr. Nicolae Spalatu and Dr. Atanas Katerski, for their serious attention to all aspects of my thesis and for the spectacular ability to give enough attention to the master students even in times of the most serious workload. I would like to thank Dr. Ilona Oja Acik (the Head of Laboratory of Thin Film Chemical Technologies) and Dr. Malle Krunks (the Director of Materials and Environmental Technology Department) for providing me the dream opportunity to dive into PV science. I sincerely appreciate the efforts of Dr. Sergei Bereznev in the supervision of our Master's program in the uncertain times of COVID-19 pandemic. I am deeply thankful to Dr. Olga Volobujeva for her help with SEM imaging. I also like to express my sincere gratitude towards Ph.D. students Robert Krautmann, Sajeesh Vadakkedath Gopi, and Nimish Juneja for their great help during this work. For me, it was an honor to study here.

This study was funded by the Estonian Research Council project PRG627 "Antimony chalcogenide thin films for next-generation semi-transparent solar cells applicable in electricity producing windows", the Estonian Research Council project PSG689 "Bismuth Chalcogenide Thin-Film Disruptive Green Solar Technology for Next Generation Photovoltaics", the Estonian Centre of Excellence project TK141 (TAR16016EK) "Advanced materials and high-technology devices for energy recuperation system", and the EU H2020 program under the ERA Chair project 5GSOLAR grant agreement No 952509.

Short summary

The thesis work focused on the post-deposition treatment (PDT) of the TiO_2 buffer layer for Sb_2Se_3 solar cells. I studied the effect of temperature and environment in the PDT of TiO_2 films on the Sb_2Se_3 film properties and TiO_2/Sb_2Se_3 solar cell performance. In the present study, glass/FTO/TiO_2/Sb_2Se_3/Au solar cells were fabricated. TiO_2 was deposited via ultrasonic spray pyrolysis (USP), post-deposition treatment included vacuum annealing (at temperatures from 120 °C to 450 °C) and air annealing (at a fixed temperature of 450 °C). Sb_2Se_3 was deposited via close-spaced sublimation (CSS). A solar cell with the highest PCE of 3.96% was obtained when TiO_2 was vacuum annealed at 160 °C and air annealed at 450 °C.

Keywords: TiO_2, post-deposition treatment, ultrasonic spray pyrolysis, Sb_2Se_3 solar cells, thin film solar cells

List of abbreviations

α-Si	Amorphous silicon
ALD	Atomic layer deposition
AsDep	As-deposited (sample)
BSE	Backscattered electrons
CdTe	Cadmium telluride
CIGS	Cadmium indium gallium selenide
c-Si	Crystalline silicon
CSP	Chemical spray pyrolisis
CSS	Close-spaced sublimation
CVD	Chemical vapor deposition
DSSC	Dye-sensitized solar cell
EDX	Energy dispersive X-rays
Eg	Band gap energy
EQE	External quantum efficiency
ETL	Electron transport layer
FGA	Forming gas atmosphere
FF	Fill factor
FTO	Fluorine-doped tin oxide
GBs	Grain boundaries
HTM	Hole transport material
ICDD	International Centre for Diffraction Data
ITO	Indium tin oxide
I_{SC}	Short circuit current
JCPDS	Joint Committee on Powder Diffraction Standards
M_{pp}	Maximum Power Point
NIR	Near infrared
P3HT	Poly(3-hexylthiophene)
PCE	Photoconversion efficiency

PCDTBT Poly [N-9’-heptadecanyl-2,7-car-bazole-alt-5,5- (4’,7’-di-2-thienyl-2’,1’,3’-benzothiadiazole)]

PDT Post deposition treatment

PLD Pulsed laser deposition

PV Photovoltaics

PVD Physical vapor deposition

RF sputtering Radio frequency sputtering

RTE Rapid thermal evaporation

Sb_2Se_3 Antimony selenide

SEM Scanning electron microscopy

SLME Spectroscopic limited maximum efficiency

TCO Transparent conductive oxide

TiO_2 Titanium dioxide

USP Ultrasonic spray pyrolysis

UV-Vis Ultraviolet-visual spectrophotometry

VE Vacuum evaporation

V_{OC} Open circuit voltage

XRD X-ray diffraction

XPS X-ray photoelectron spectroscopy

ZnO Zinc oxide

INTRODUCTION

The sun is responsible for nearly all the energy on Earth. The exceptions are attributable to moon-related tidal energy, nuclear energy, and geothermal energy. Everything else is a converted form of the sun's energy: Hydropower is made possible by evaporation-transpiration due to solar radiant heat; the winds are caused by the sun's uneven heating of the Earth's atmosphere; fossil fuels are remnants of organic life previously nourished by the sun. Finally, photovoltaic electricity is produced directly from sunlight by converting the energy of the sunlight into free-charged particles within certain kinds of materials [1].

Implementation of solar energy sources, as well as other renewables, is a crucial way to satisfy the increasing energy demand – without unnecessary carbon emissions.

According to International Renewable Energy Agency (IRENA) annual report "Renewable Capacity Statistics 2021", in 2020, global cumulative solar capacity was above 713 GW – and 126 GW were installed during the last year [2]. However, it still makes only 2% of global energy production [3]. To achieve the UN target goal 7 (Affordable and clean energy) until the year 2030 [4] and aims of the Paris agreement until 2050 [5], the current growth rates of this industry are insufficient. One way to decrease the price of solar panels and, consequently, increase the growth rates of a solar industry is the diversification of the solar cell market. About 95% of the market is occupied by mono- and polycrystalline silicon (mono-Si and poly-Si), with a 5% share for all thin film technologies combined [6].

On an industrial scale, other notable thin film solar cell technologies include CIGS (copper indium gallium selenide), CdTe (cadmium telluride), and ɑ-Si (amorphous silicon). The current efficiencies of CIGS and CdTe are 23.4% and 22.1%, respectively, which are comparable to polycrystalline (22.3%) but lower than the mono-Si (26.1%)[7]. At the same time, thin film cell manufacturing requires less material, lower energy, and has higher resource savings potential [8]. However, the high price for indium (In) and toxicity of cadmium (Cd) and tellurium (Cd)have intensified research into alternative thin film absorber materials [9]. One of the perspective materials is Sb_2Se_3, which combines suitable optoelectronic characteristics, higher abundance, low toxicity, and compatibility with CdTe manufacturing processes [9].

Herein the systematical investigation of the effects of TiO_2 vacuum annealing procedure on TiO_2 buffer and Sb_2Se_3 absorber layer properties and the Glass/FTO/TiO_2/Sb_2Se_3/Au solar cell performance was conducted. Insights into the processes leading to the changes in the properties of annealed TiO_2 films and TiO_2/Sb_2Se_3 thin film solar cells are proposed.

The work comprises a theoretical background of solar cells, materials involved in the study, and a description of deposition and characterization techniques. The second part presents an overview of the experimental part: the deposition and the PDT of TiO_2 buffer and

the deposition of Sb_2Se_3 absorber. The experimental section also covers the material and device characterization, e.g., scanning electron microscopy (SEM), X-ray photoelectron spectroscopy (XPS), and current-voltage (J-V) characteristics. The third part includes results and discussion.

1. THEORETICAL BACKGROUND

1.1. The basics of solar cells

The photovoltaic effect was first time demonstrated in 1839 by Edmond Becquerel and named in 1849 by Alfred Smee [10]. The first semiconductor (selenium) solar cell was constructed in 1883 by Charles Fritts. It is notable that all these achievements happened long before electron existence was proved (1897, by Joseph Thompson). Overall, the theoretic apparatus for the PV effect studies were developed during the first half of the 20th century (Max Planck, Walter Schottky, etc.). The first modern-type PV cell made of silicon was developed and patented in 1941-1946 by Russel Ohl. However, the first silicon cells with 4% efficiency were manufactured only in 1953 by Calvin Fuller.

A solar cell is a device made of two semiconductor materials, which can absorb light and convert the energy of the absorbed photons to electric current [11]. Junction between n-type (with the excess of electrons) and p-type (with the excess of holes) semiconductor has an electric potential, which sweeps charge carriers away out from the junction and into the external circuit. . The process of current generation consists of photon absorption, electron-hole pair separation, and charge collection. Figure 1 schematically depicts these three steps of the current generation.

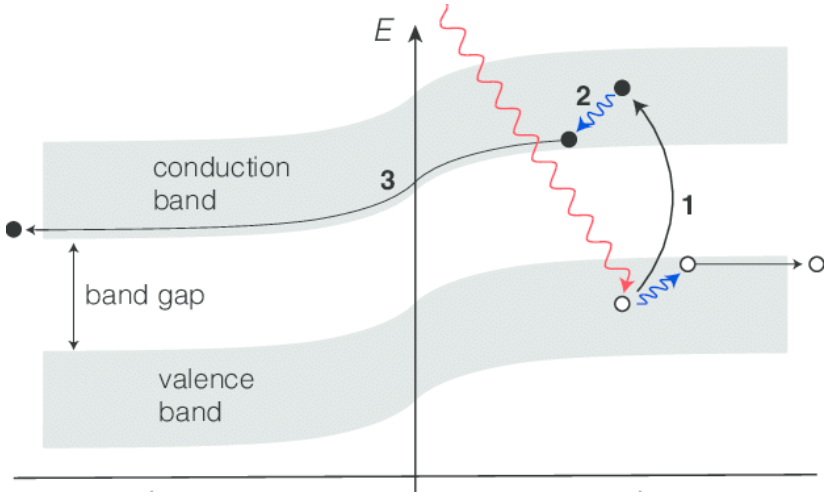

Fig. 1. Illustration of the photovoltaic effect. 1. A photon is absorbed in the p-type phase of the semiconductor, generating a conducting pair (electron and hole). 2. The pair quickly thermalizes with the phonons in the lattice, dissipating the energy excess above the band gap. 3. The electron is driven to the left by the potential difference across the interface, while the hole moves to the right, generating voltage between two terminals [12].

Silicon is the most widely used photovoltaic absorber material. Silicon is naturally intrinsic but can be made n- or p-type through doping. To get n-type silicon, it is doped with donor atoms, which have more electrons - like P or As (group V, 5 e^-). Vice versa, to achieve p-type conductivity, silicon is doped with acceptor atoms, which have fewer electrons – like B (group III, 3 e^-). If a p-n junction is created using a single material, which is typical for silicon solar cells, it is called a homojunction. Thin film solar cells mostly have heterojunctions, as the junction is formed between two different materials, e.g., CdS/CdTe, ZnO/CIGS, or WS_2/CIGS [11]. In the case of the CdS/CdTe junction, the CdS buffer is naturally n-type due to sulfur vacancies, and the CdTe absorber is p-type owing to its cadmium vacancies [13][14]. In the TiO_2/Sb_2Se_3 cells studied in this thesis, TiO_2 buffer is n-type due to oxygen vacancies, while Sb_2Se_3 is p-type most likely because of antimony vacancies and selenium antisite defects [15].

1.1.1. Thin film solar cell configuration

Thin film solar cell usually consists of a p-n junction formed between n-type buffer and p-type absorber material, or a p-i-n junction formed between n-type electron transport layer (ETL), intrinsic absorber, and p-type hole transport material (HTM). The p-n junction is sandwiched between a front contact and a back contact, which are good electric conductors to guide the charge carriers into the external circuit readily. In thin film solar cells, the front contact is transparent because it must allow the light to pass through towards the absorber layer. Transparent conductive oxides (TCO), such as fluorine-doped tin oxide (FTO) and indium-doped tin oxide (ITO), are typically used as front contacts. They both have high transparency (80%) and boast low sheet resistance (< 30 Ω/sq) [13].

A buffer layer is, in general, an n-type semiconductor with a wide band gap and high transparency. The main role of the buffer layer is to reduce the lattice mismatch between the absorber and front contact. It is also essential that the buffer is more conductive than the absorber. In that case, the depletion region extends more into the absorber, where most of the charge carriers are generated. Standard options in the thin film industry are CdS, TiO_2, ZnO with various doping [9][16].

The absorber layer is generally a p-type semiconductor. It has a lower band gap (mainly between 1-2 eV [17]) and high absorption coefficient (> 10^4 in the visible and NIR range [18]). The absorber is the layer where photocarriers are generated, then swept away by the depletion region. The most well-known absorber layer materials for thin film solar cells are CdTe, CIGS, a-Si, kesterites, and perovskites.

Back contact is usually a metal contact. Gold (Au), molybdenum (Mo), and copper (Cu) are most commonly used. Back contact extracts the charge to the external load. It should also

have a suitable electronic work function to avoid potential roll-over effect at the back surface of the solar cell [13].

There are two configurations for thin film solar cells – superstrate and substrate (Fig. 2). In the superstrate configuration, TCO-coated glass forms the substrate onto which buffer layer is deposited. It is followed by the absorber layer and back contact. In the substrate configuration, the back contact is the substrate that is deposited on the glass. Next, the absorber layer is deposited, followed by the deposition of the buffer layer and TCO.

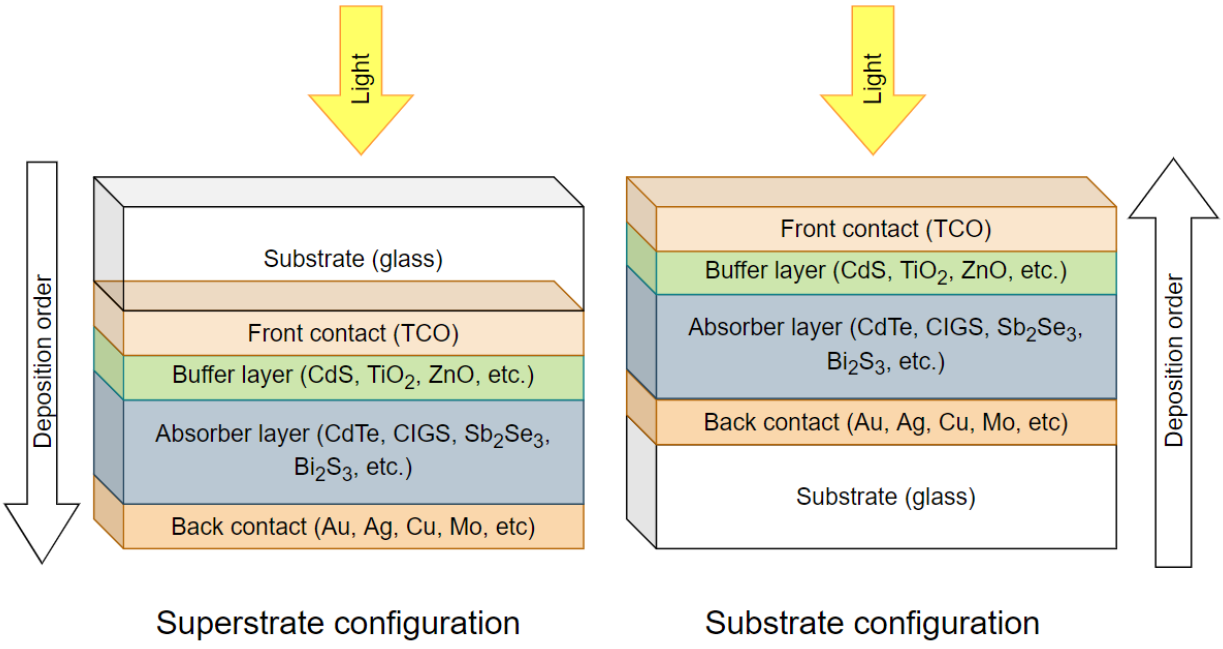

Fig. 2. Schematic of thin film solar cell configurations.

1.1.2. Three generations of the photovoltaic

Solar cell technologies can be divided into three generations. The first-generation PV is based on silicon, the second most abundant element in the Earth's crust. Today, most of the solar panels on the market are made of either poly-Si, which are cheaper to produce, or mono-Si, which offers better power output compared to the poly-Si solar cells. Current maximum efficiencies are – 22.8% and 26.7% for poly-Si and mono-Si solar cells, respectively[19].

The second-generation PV is an umbrella term covering three thin film solar cell manufacturing technologies – CdTe, CIGS, and amorphous silicon. Current efficiencies in laboratory conditions are as follows: PCE of 21% for CdTe, PCE of 23. % for CIGS, PCE of

10.2% for α-Si. As can be seen, these technologies have not been able to outperform the silicon solar cell technologies and grab a larger market share, as seen in Fig. 3. Moreover, they are experiencing other drawbacks. For instance, the scarcity of indium (In) is limiting CIGS solar cell production, and there is a significant environmental concern over the toxicity of Cd and Te [20]. Therefore, other binary chalcogenide compounds, such as FeS_2, Cu_2S, SnS, or Sb_2Se_3, which belong to the 3rd generation materials, are now being explored that could be adapted to the well-established manufacturing processes of CdTe and CIGS.

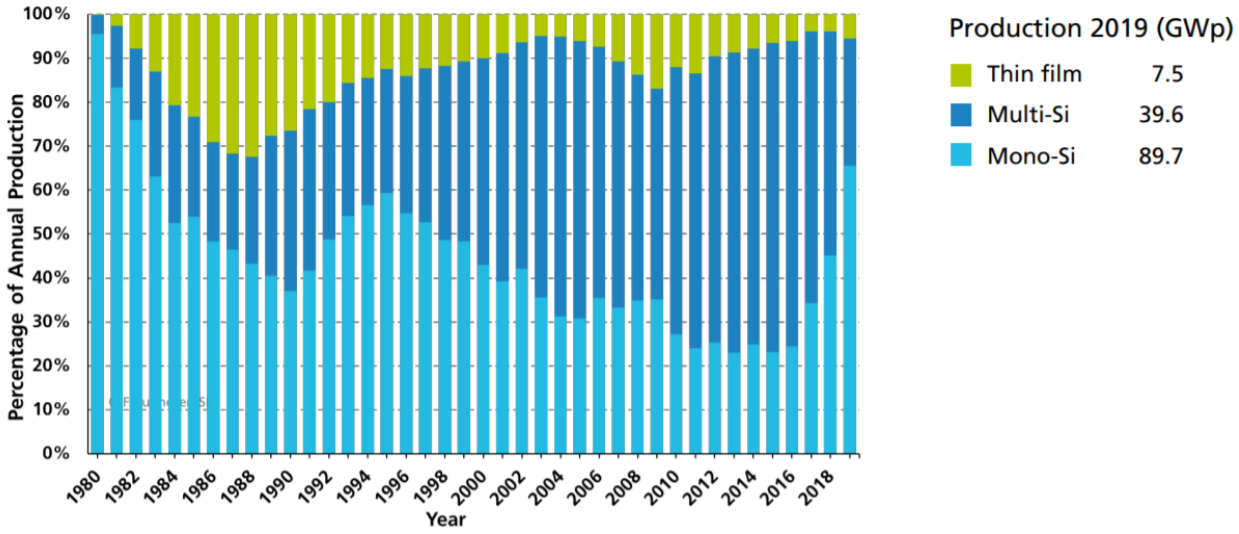

Fig. 3. Global market share of PV technologies – the percentage of global annual production [21].

The third generation of PV is an umbrella term for all emerging technologies, including perovskite solar cells (PSC), organic solar cells (OSC) cells, quantum dot solar cells (QDSC), dye-sensitized cells (DSSC), and chalcogenide solar cells, such as kesterites and $Sb_2(S,Se)_3$ solar cells [22].

1.1.3. Antimony selenide

This work focuses on antimony selenide (Sb_2Se_3), one of the most promising emerging absorber materials. As well as CdTe, it is a single-phase V-VI binary material, with a direct band gap of 1.1–1.3 eV [16]. The theoretical absorption coefficient was found to be $>10^4$ cm^{-1} for energies above 1.5 eV, increasing to 1×10^5 cm^{-1} at 1.8 eV, indicating a sharp and strong absorption edge [16]. Carrier mobility is near 10 $cm^2V^{-1}s^{-1}$ [23][24][25]. Unlike the case of CdTe, compounds of Sb_2Se_3 are relatively abundant and non-toxic [26]. Sb_2Se_3 exhibits an orthorhombic crystal structure and a tendency to form ribbon-like one-dimensional (1D)

structures, which consists of covalently stacked $(Sb_4Se_6)_n$ blocks[27][28]. These ribbons are connected through van der Waals forces[29], which is believed to reduce the density of dangling bonds at the grain boundaries (GB) [30].

In the case of untreated, as-deposited cells, Sb_2Se_3 absorber tends to outperform CdTe absorber, which could be attributed to their difference in photosensitivity and resistivity [31]. Also, in terms of spectroscopic limited maximum efficiency (SLME) [32] of Sb_2Se_3 outperforms both CZTS and CdTe, having 28.2% already at a thickness of 200 nm, comparing with 21.5% and 20.3%, respectively, which could look promising from the point of resource-efficient manufacturing of solar cells [16].

Low melting point [33] and high vapor pressure of Sb and Se [34]allow the use of a wide range of deposition techniques, such as magnetron sputtering, vacuum evaporation (VE), close-spaced sublimation (CSS), and chemical methods [9][35].

1.1.4. Review of Sb_2Se_3-based PV

The first found solar cell based on Sb_2Se_3 absorber, reported in 2009 achieved PCE of 0.66%[36]. In 2013 [37], Sb_2Se_3 was employed in a DSSC, achieving 3.21% efficiency[37]. The efficiency of 5.6% was achieved in 2015 for glass/FTO/CdS/Sb_2Se_3/Au stack, using RTE (rapid thermal evaporation)[34]. In 2018 the cell with 6.6% efficiency was made, where PCDTBT (poly [N-9’-heptadecanyl-2,7-car-bazole-alt-5,5- (4’,7’-di-2-thienyl-2’,1’,3’-benzothiadiazole)]) organic layer was included between Sb_2Se_3 absorber and Au back contact [38]. In 2018, a solar cell employing Sb_2Se_3, which was deposited by vapor transport deposition (VTD), showed PCE of 7.6% [25].

The next significant leap in terms of efficiency was done in 2019. Substrate Sb_2Se_3 solar cell structure (ZnO:Al/ZnO/CdS/TiO_2/Sb_2Se_3nanorod arrays/$MoSe_2$/Mo) was produced, with ALD-deposited TiO_2 and CSS-deposited Sb_2Se_3, which altogether led to the PCE of 9.2% [24]. It was the last record in the area of pure Sb_2Se_3 as an absorber. In 2020 the most efficient cell with TiO_2/Sb_2Se_3 was manufactured, showing 7.3% efficiency [39]. In 2020, two groups showed results with 10% and 10.5% efficiency. Both of them used chemically-deposited antimony selenosulfide $Sb_2(S,Se)_3$ intending to optimize the S/Se ratio within the absorber layer [40][41].

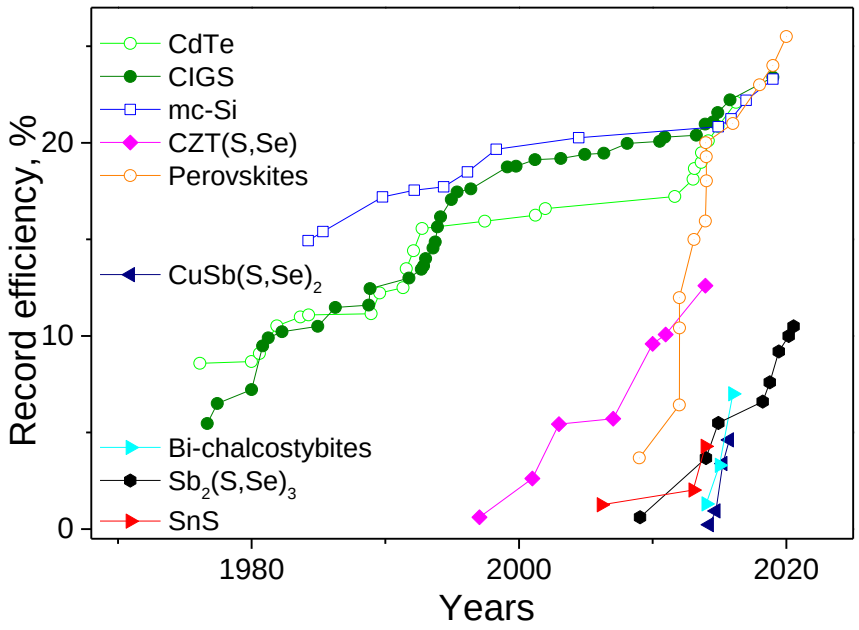

Fig. 4. Development of emerging photovoltaic absorbers. Redrawn form [42], updated using sources [25][24][38][40][41][43][44][45].

1.1.5 Titanium dioxide

As shown above, titanium dioxide (TiO_2) is a suitable buffer layer in the Sb_2Se_3 solar cell. TiO_2 is a wide band gap semiconductor with a band gap at 2.8–3.3 eV, which is larger than in CdS (E_g = 2.5 eV) [46]. In nature, crystalline TiO_2 can be found having phases of either anatase, rutile (tetragonal crystal structure), or brookite (orthorhombic), as seen in Fig. 5 [47]. It has found significant use in different established and emerging technologies, such as in c-Si [48], CdTe [49], CZTS [50], and more recently in perovskites and chalcogenide solar cells [51]. The ΔG of the reaction between TiO_2 and Sb_2Se_3 is largely positive, indicating a thermodynamically unfavorable reaction in the system, which in theory should provide better lattice matching [9]. TiO_2 thin films can be produced by various techniques, such as vacuum-based techniques, e.g., sputtering, atomic layer deposition (ALD), pulsed laser deposition (PLD), and chemical vapor deposition (CVD) and solution-based techniques, e.g., sol-gel, spin-coating, and spray pyrolysis [52]. The most efficient TiO_2/Sb_2Se_3 solar cell demonstrated an efficiency of 7.3% [39].

In most cases, TiO_2 in thin film PV studies is deposited via chemical methods. Currently, TiO_2 is most actively used in the perovskite industry. After deposition, the most common PDT way for TiO_2 is to anneal it in air atmosphere at 450-500 °C for 30-60 minutes. Table 1 summarizes research efforts in the literature on deposition and annealing procedures for TiO_2 films and its

integration in various types of solar cells. The primary purpose of air annealing was to provide crystallization to the TiO_2 film. The influence of the organic residuals in the film was less considered, despite their destructive potential for the film [9]. It was usually supposed that nearly all the organic, which was used at the step of deposition (such as precursor solutions), burns out at the step of deposition or, later, at the step of the subsequent air annealing. However, recent findings of our laboratory stated [9] that even after conventional air annealing treatment, organic residuals may be present in the USP-TiO_2 film and stay harmful for solar cell operational characteristics.

Table 1. TiO_2 deposition and annealing procedures through the researched literature.

Year	Cell composition	TiO_2 deposition technique	TiO_2 annealing procedure	Absorber	PCE, %	Ref.
2016	Al_2O_3/c-Si/SiO_2/TiO_2/Al	ALD	250 °C FGA annealing, 3 min	c-Si	17.6-21.6	[48]
2016	glass/ITO/TiO_2/Sb_2S_3/P3HT/Au	CSP	450 °C air annealing, 30 min	Sb_2S_3	1.3	[53]
2017	ZnO/TiO_2/Sb_2S_3/P3HT/Au	ALD	300 °C air annealing, 3 hours	Sb_2Se_3	2.3	[54]
2018	FTO/TiO_2/CdS/CdTe/Au	Sol-gel deposition	500 °C air annealing, 1 hour	CdTe	5.16	[49]
2018	FTO/TiO_2/$PC_{61}BM$/ $CH_3NH_3PbI_{3-x}Cl_x$/HTM/Ag	Spin coating	500 °C air annealing, 15 min	Perovskite	18.3	[51]
2019	ZnO:Al/ZnO/CdS/TiO_2/Sb_2Se_3 nanorod arrays/$MoSe_2$/Mo	ALD	No annealing	Sb_2Se_3	9.2	[24]
2019	FTO/BL-TiO_2/ns-TiO_2/SnS/Au	CSP	500 °C air annealing, 1 hour	SnS	4.8	[55]
2020	FTO/ TiO_2/CdS/CZTS/Au	Hydrothermal	450 °C air annealing, 1 hour	CZTS	1.04	[50]
2020	glass/FTO/TiO_2/Sb_2Se_3/Au	RF sputtering + spin-coating	500 °C air annealing, 30 min	Sb_2Se_3	7.3	[39]
2021	FTO/USP-TiO_2/Sb_2Se_3/Au	USP	450 °C air annealing, 30 min	Sb_2Se_3	5.3	[9]
2021	m-TiO_2/ C-Chl/$Cs_2AgBiBr_6$/HTM/Au	Water bath	120 °C air annealing, 2 hours	Perovskite	21.16	[56]

One solution for expulsing these organic residuals from TiO_2 films and improving their optoelectronic properties is to apply the controlled thermal annealing in relevant ambient conditions[13]. A similar mechanism was previously observed with oxygen impurities in CdS/CdTe solar cells [57], and it may be also possible for TiO_2. Therefore, a thorough study of the influence of TiO_2 buffer layer PDT procedure on the concentration of carbon in TiO_2 film and the efficiency of the solar cell should be provided.

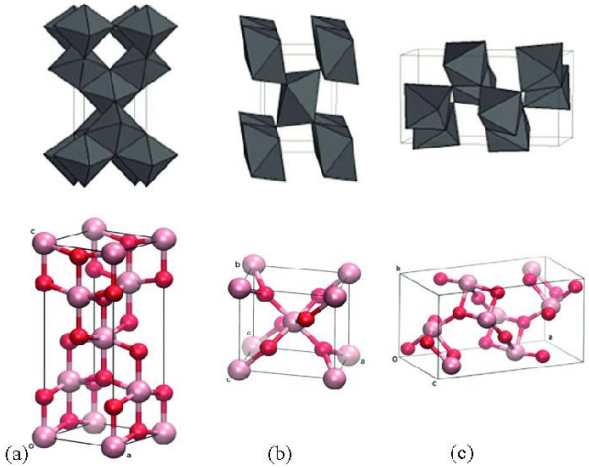

Fig. 5. Crystal structures of TiO_2 : (a) anatase, (b) rutile, and (c) brookite [58].

1.2. Material deposition methods for absorber and buffer layers

During this work, two main deposition methods were used – close-spaced sublimation (CSS), a physical vapor deposition (PVD) method, and ultrasonic spray pyrolysis (USP), which is a chemical method. In the beginning, USP was used for TiO_2 deposition on glass/FTO substrate. After post-deposition procedures, the Sb_2Se_3 absorber was deposited atop of this TiO_2 by CSS method.

1.2.1. Close-spaced sublimation (CSS)

As well as in other methods of PVD family, during the deposition by CSS method material experiencing two-phase changes (Fig. 6.1) – sublimation (from solid-state to gaseous phase) and desublimation (from gaseous to solid). Solid or liquid material is heated up to the vaporization point. Then, vapor crosses the gap between the source and substrate according to the temperature gradient and condenses on its surface. The deposition should be done in a high vacuum to prevent contamination and interruption of vapor flow by gas particles. The principal scheme of the PVD process is shown in Fig.6a

The central otherness of CSS (comparing with other PVD methods) lies in the minimal (in general 2-20 mm) distance between source and sample. These are encapsulated in a small common volume, which imitates the conditions of a sealed ampoule. The scheme of the CSS process is shown in Fig. 6.b.

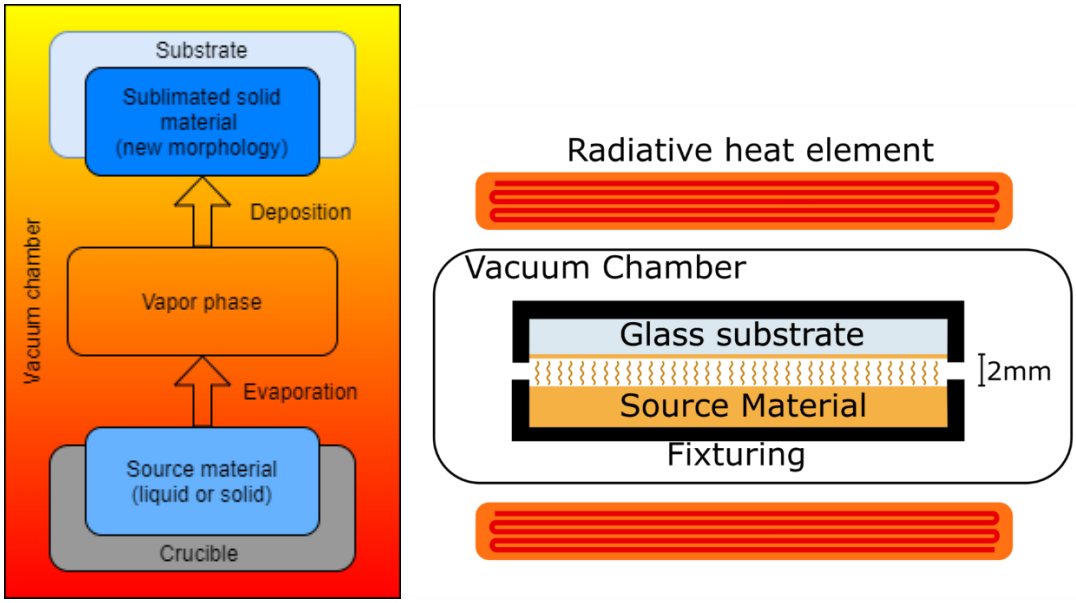

Fig. 6.a – principal scheme of PVD family of methods. **6.b** – principal scheme of CSS reactor.

A custom CSS system used in this study was designed to maintain a high-purity deposition condition. The schematic diagram of the system is shown in Fig.6.1. The system consists of two graphite cylinders stacked vertically on top and the bottom of a stainless-steel cylindrical tube. A quartz tube is positioned within a cylindrical hole in the bottom block, referred to as the source graphite block. A substrate block is placed on top of the steel tube; a quartz crucible was used to hold the source material and provide separation between the source and the substrate graphite blocks. Tungsten coil heaters provide heating for both the source and substrate blocks. Thermocouples are inserted inside both graphite blocks to control the temperature. The temperatures recorded for the substrate and source graphite blocks are assumed to be the actual temperatures of the substrate and the source material, respectively. The heaters are individually controlled to set the desired temperature gradient in the system [13].

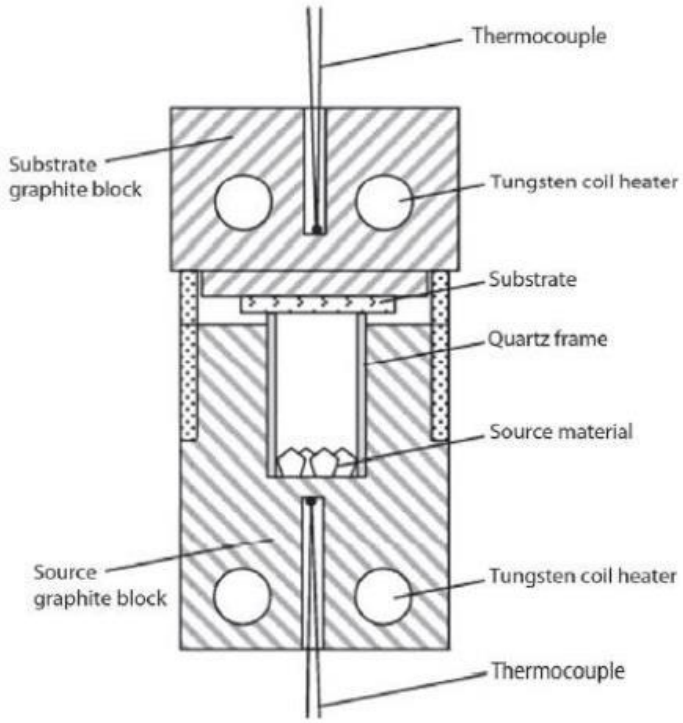

Fig. 7. Schematic representation of used CSS system.

Before deposition, the reaction chamber is evacuated to attain a high vacuum. First, a rotary oil pump applied to decrease the pressure under the dome from the ambient atmosphere to the 10^{-4} Torr. Then, the diffusion pump is applied decrease the pressure further to of 10^{-6} Torr. During the deposition, the source material is heated up to the sublimation temperature. The substrate is also heated, but to the a bit lower temperature, to create the temperature

gradient from the source to the substrate. The crystallinity of the thin films depends on the distance between the source and substrate, evaporation and substrate temperature, and background gas pressure [59][60].

1.2.2. Ultrasonic spray pyrolysis (USP)

The ultrasonic spray pyrolysis (USP) is a simple, continuous, scalable, and cost-efficient deposition method [35]. Suits for metal oxide deposition. On the first step of the procedure, the precursor solution is nebulized in the ultrasonic wave generator to create droplets with a suitable size (usually less than 20 μm). Next, droplets are guided by the pumped gas flow towards the substrate, which lies onto the hot plate. Solvent (deionized water, alcohol, or another liquid) evaporates, organic compounds are decomposing, and only desirable metal oxide thin film stays on the substrate [61][60].

Figure 8 shows the principal scheme of the ultrasonic spray pyrolysis setup. The precursor solution is placed into a closed chamber (also called nebulizer) with an ultrasonic generator, where ultrasonication is performed to create fine droplets of the solution[62]. Piezo crystals of the generator are oscillating at high frequency, creating stationary waves inside the precursor solution and initiating rapid vaporization[63]. The higher is oscillation frequency - the finer are the droplets. Then, deposition of the finer droplets results in considerably more homogenous film [63][64][60]. After the formation of vapor, it is subsequently guided through the nozzle towards the heat plate with the aid of transport gas (usually compressed air). The hot plate heats the substrate to the temperature desired for the specific thin film deposition. The track of the nozzle above the plate is pre-programmed to make the film more homogenous.

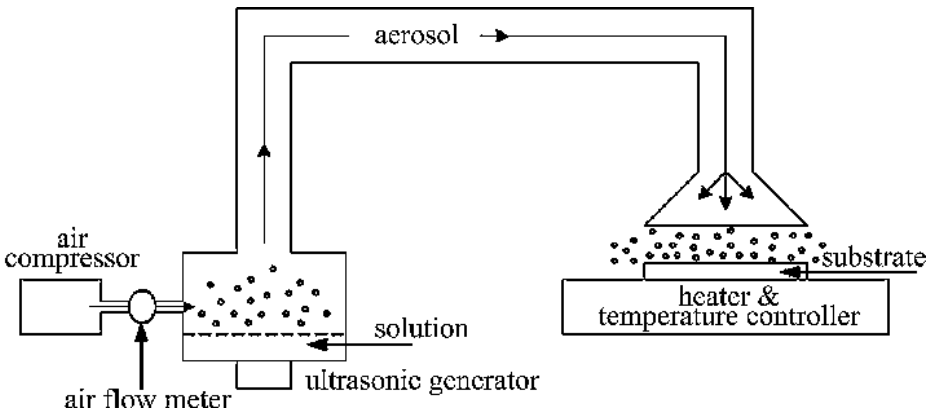

Fig. 8. Principal scheme of the setup for ultrasonic spray pyrolysis [65].

During the USP deposition, evaporation of the solvent, organic decomposition, and grain growth relates to the temperature of the substrate [63], which is therefore considered the most critical parameter of the process[66]. Also, ambient pressure and spray rate are considered as influencing the process. Other parameters, such as the ambient pressure, nozzle-to-substrate distance, spray rate, carrier gas flow rate, concentration of precursor solution, and evaporation rate, should be carefully fitted to achieve a the film with desired characteristics [60].

1.3. Material characterization methods

1.3.1. X-ray diffraction (XRD)

X-ray diffraction is a powerful nondestructive technique for characterizing crystalline materials. It provides information on structures, phases, preferred crystal orientations (texture), and other structural parameters, such as average grain size, crystallinity, strain, and crystal defects [67]. X-ray diffraction means the effect of elastic scattering of x-ray photons by atoms in a periodic lattice. The scattered monochromatic x-rays that are in phase give constructive interference. Figure 1 illustrates how diffraction of x-rays by crystal planes allows one to derive lattice spacings using Bragg's law [68].

$$n\lambda = 2d \sin \theta \quad (1)$$

where n is an integer called the order of reflection, λ is the wavelength of x-rays, d is the characteristic spacing between the crystal planes of a specimen, and θ is an angle between the incident beam and the normal to the reflecting lattice plane.

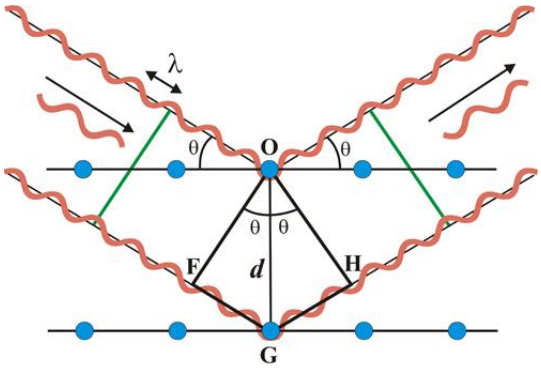

Fig. 9. Principle of X-ray diffraction [69].

By measuring the angles, θ, under which the constructively interfering x-rays leave the crystal, the interplanar spacings, d, of every single crystallographic phase can be determined. To identify an unknown substance, the powder diffraction pattern is recorded with the help of

a camera or a diffractometer. A list of d-values and the relative intensities of the diffraction lines are prepared.

To get the information about the preferential orientation of the crystallites in the film, these data are compared with the standard line patterns for various compounds in the Powder Diffraction File (PDF) database. This file is released and annually updated by the International Centre for Diffraction Data (ICDD), also known as Joint Committee on Powder Diffraction Standards (JCPDS)

1.3.2. UV-VIS spectrophotometry

UV-Vis Spectroscopy (or Spectrophotometry) was used to determine the optical band gap of the samples. It is a quantitative technique for determining how much light is absorbed by a chemical substance. It is accomplished by measuring the intensity of light passing through a sample to passing through a reference sample or blank. This technique can be applied to various samples, including liquids, solids, thin films, and glass [70]. Two radiation intervals are used, specifically ultraviolet (UV 300 to 400 nm) and visible (vis, 400 to 765 mm). UV-Vis spectrophotometry makes it possible to describe thin film optical parameters such as transmittance, reflectance, and absorbance. Basing on these parameters, thickness, absorption coefficient, and band gap of the film may be calculated. Transmittance and reflectance spectra are measured using an integrated sphere (Fig. 10).

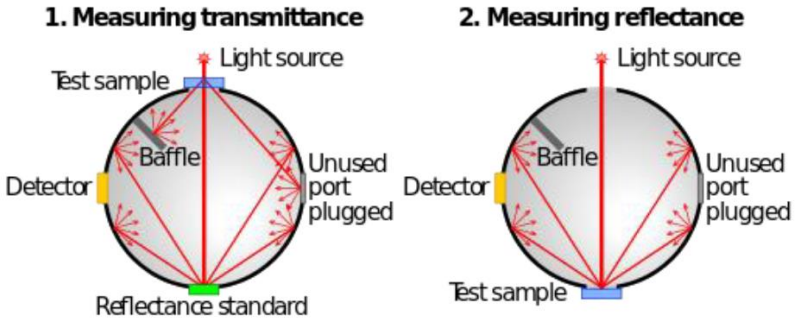

Fig. 10. Transmittance and reflectance modes in UV-vis spectrometry [71].

Transmittance and reflectance spectra can be evaluated by dividing transmitted or reflected light to the incident light[59]. Based on these spectra, the absorption coefficient, α, can be obtained, using the equation (2):

$$\frac{T}{100-R} = e^{-\alpha d} \quad (2)$$

Where d is equal to the thickness of the film.

The optical band gap is calculated using Tauc relation, which connects derived absorption coefficient with band gap (3):

$$(\alpha hv)^n = A(hv - E_g) \quad (3)$$

where A is a constant, h is Planck's constant, v is light frequency, and E_g is an optical band gap [71].

1.3.3. Scanning electron microscopy (SEM)

To get detailed pictures of the film, the SEM technique was involved. SEM images the sample surface by scanning it with a high-energy beam of electrons in a raster scan pattern. The primary electron beam produced under a high vacuum scans across the surface of a specimen. When the electrons strike the specimen, a variation of the signal produces an image of the surface or its elemental composition together with energy dispersive X-rays (EDX) [72].
The concept of scanning electron microscope is depicted in Figure 11.

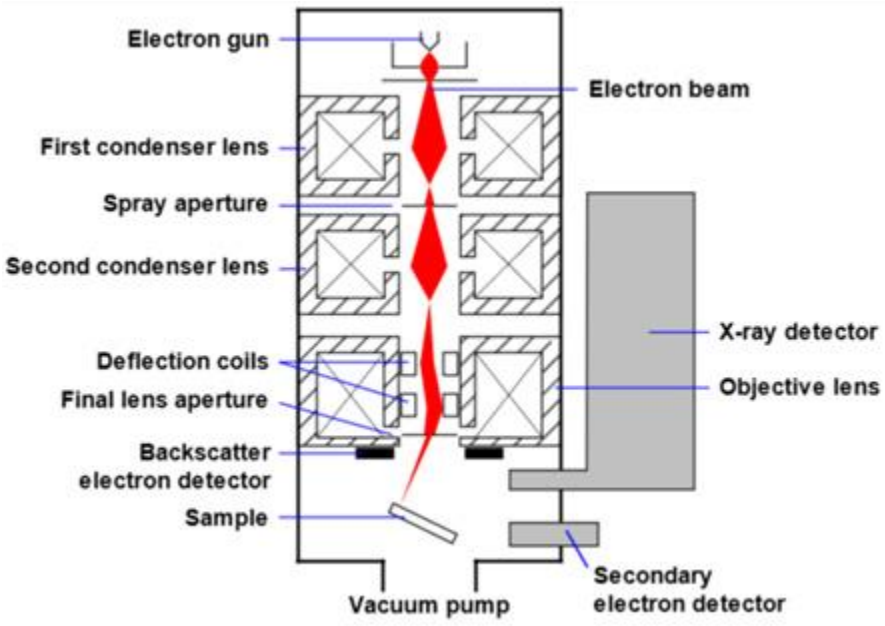

Fig.11. The scheme of scanning electron microscope [73].

The main SEM components include a source of electrons, column down which electrons travel with electromagnetic lenses, electron detector, sample chamber and a controlling unit [73].

Electrons are produced at the top of the column, accelerated down, and passed through a combination of lenses and apertures to produce a focused beam of electrons that hits the surface of the sample. The sample is mounted on a stage in the chamber area. Unless the microscope is specifically designed to operate at a low vacuum, both column and chamber are evacuated by a combination of pumps. The level of the vacuum will depend on the design of the microscope [73].

The electron beam position on the sample is controlled by scan coils situated above the objective lens. These coils allow the beam to be scanned over the surface of the sample. This beam rastering or scanning, as the name of the microscope suggests, enables information about a defined area on the sample to be collected[74]. As a result of the electron-sample interaction, signals are produced. These signals are then detected by appropriate detectors [73].

Several functions have been developed with the principles of SEM to have a better understanding of material surfaces. Backscattered electrons (BSE) are electrons that are reflected from the sample by elastic scattering. BSE images can provide information about the distribution of different elements in the sample according to their atomic number. Field emission guns SEM (FEG SEM) enables a higher resolution and magnification, which is widely used in nanotechnology and biomedical fields [73].

1.3.4. X-ray photoelectron spectroscopy (XPS)

X-ray photoelectron spectroscopy (XPS) is a quantitative technique for measuring the elemental composition of the surface of a material. It can also determine the binding states of the elements. It involves detecting photoelectrons emitted from a sample as a result of irradiation of the sample by single-energy X-ray photons [75]. Here, XPS was involved in examining the surface layer of the TiO2 film for carbon impurities, which were not seen using other methods.

Slight variations in binding energies of the photoelectron lines, Auger lines, satellite peaks, and multiple splitting can be used to identify chemical states. XPS is initiated by irradiating a sample with monoenergetic soft X-rays, most commonly Mg Kα (1253.6 eV with a line width≈0.7 eV) or Al Kα (1486.6 eV with a line width ≈ 0.85 eV). In many modern instruments, the Al Kα X-ray line is further narrowed (to≈0.35 eV) using a monochromator[76].

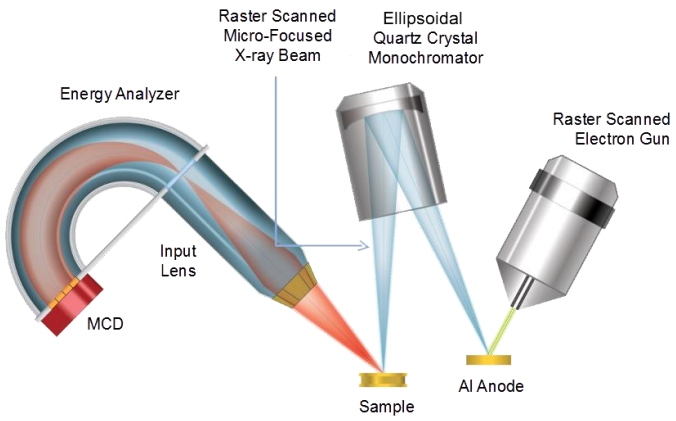

Fig 12. A simplified picture of X-ray photoelectron spectroscope [77].

XPS is helpful for quantitative analysis of surface composition and can detect all elements except for hydrogen and helium through the detection of the binding energies of the photoelectrons.

XPS normally probes to a depth of 5-10 nm. XPS is an ultra-high vacuum technique, so the sample to be analyzed has first to be evacuated [78].

1.4. Solar cell characterization techniques

1.4.1. Current density-voltage (J-V)

The current density-voltage (J-V) characteristic is the main method to find the quality of the solar cell. Solar cell exhibits the properties of a diode, which produces current under illumination (due to photovoltaic effect) [79]. When the current (in the case of PV – photocurrent) flows through the p-n junction, the solar cell biases itself, therefore reducing the electrostatic barrier and increasing diode current. Diode current flows in the opposite direction (so it also calls reverse current). Under negative bias ($V_{bi} < 0$), diode current is neglectable but rises exponentially under positive bias ($V_{bi} > 0$) [60].

In the case of the ideal diode model, external photocurrent (J_{sc}, photocurrent, generated in short circuit conditions or short-circuit current) can be calculated according to equation 4.

$$J(V) = J_0 \left(e^{\frac{qV_{bi}}{k_B T}} - 1 \right) - J_{sc} \tag{4}$$

Where J_0 is reverse saturation current, k_B is Boltzmann constant, q is elemental charge in C, T is the temperature in kelvins, V_{bi} is applied bias in V and J_{sc} is a short circuit current density in mA/cm^2 [11][79].

When cell is illuminated, but not connected to the external circuit, V_{bi} increases up to the moment when the diode current cancels out the generated photocurrent. This signals about the maximum possible bias, which is called open-circuit voltage (V_{oc}, V) [60]. For the ideal diode model, V_{oc} can be calculated from equation 5:

$$Voc = \frac{kT}{q} ln\left(\frac{J_{sc}}{J_0} + 1\right) \quad (5)$$

where J_{sc} is the short circuit current density in mA/cm^2, J_0 is the reverse saturation current, q is elemental charge in C, k is Boltzmann constant, and T is the temperature in kelvins [79].
Fill factor (FF) could be interpreted as a "measure of squareness" of the J-V characteristic. It reflects the effects of series and shunt resistance. Series resistance is the result of the resistivity of materials and contact regions, which hinder charge flow. High series resistance should be low to maintain the charge collection uninterrupted. Shunt resistance reflects the parasitic current routes within the cell, for example a direct connection between front and back contacts. It should be as large as possible to increase the external photocurrent [79][60]. FF is a ratio, shown in equation 6:

$$FF = \frac{J_{mp} \times V_{mp}}{J_{sc} \times V_{oc}} \quad (6)$$

where J_{mp} is the maximum point for current density in mA/cm^2, V_{mp} is the maximum point for voltage in V, J_{sc} is short circuit current density, and V_{oc} is open-circuit voltage [79][60].
Figure 13 depicts an J-V characteristic of the solar cell, which was measured in the dark and illuminated conditions. In the dark, when the forward bias is applied, there is only a diode current. Under illumination, there is also an external photocurrent that flows in the opposite direction, comparing with diode current and therefore having a negative value. J_{mp} and V_{mp} from the equation AAQ describe the maximum power point of the J-V curve. Thus, the power density P of solar cell can be calculated as equation 7:

$$P = FF \times J_{SC} \times V_{OC} = J_{mp} \times V_{MP} \quad (7)$$

Photoconversion efficiency (PCE, also can be written as η) is the main parameter of the solar cell that defines the relationship between the maximum power density of the cell to the solar irradiance, which can be calculated from 8 equation:

$$PCE = \frac{J_{mp} \times V_{MP}}{P_s} \quad (8)$$

Where P_s is the solar irradiance in W/m^2 [79][60].

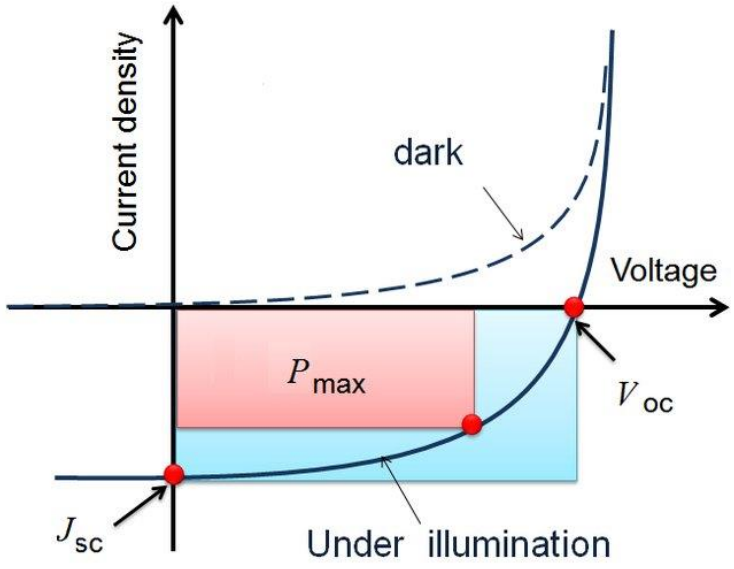

Fig.13. J-V characteristics of a solar cell measured in the dark and illuminated conditions [60][80].

1.4.2. External quantum efficiency (EQE)

The "quantum efficiency" is the ratio of the number of carriers collected by the solar cell to the number of photons of a given energy incident on the solar cell. The quantum efficiency may be given either as a function of wavelength or as energy [81]. If all photons of a certain wavelength are absorbed, and the resulting minority carriers are collected, then the quantum efficiency at that particular wavelength is equal to 1. The quantum efficiency for photons with energy below the band gap is zero. A quantum efficiency curve for an ideal solar cell is shown below [81].

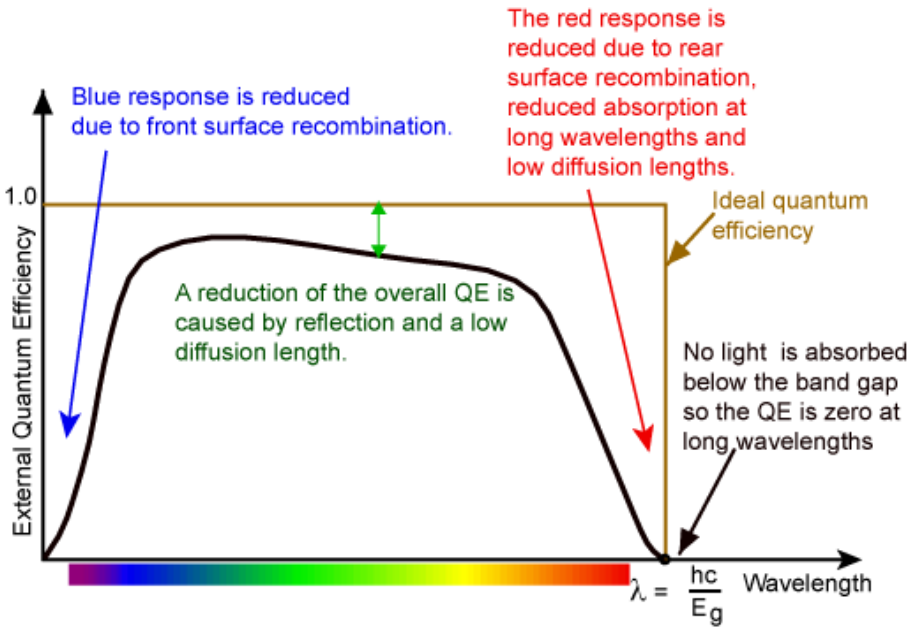

Fig.14. The quantum efficiency of a silicon solar cell. Quantum efficiency is usually not measured much below 350 nm as the power from the AM1.5 contained in such low wavelengths is low [81].

1.5. Summary of theoretical background and aims of the thesis

Based on the literature, the following features should be considered:

1. Antimony selenide (Sb_2Se_3) is a promising absorber, exhibiting a suitable band gap and high absorption coefficient. Sb_2Se_3 cells achieved an efficiency of 9.2%, and $Sb_2(S,Se)_3$ cells are at 10.5% now.
2. The state-of-the-art Sb_2Se_3 cells have been fabricated using physical deposition methods, such as close-spaced sublimation (CSS) and vapor transport deposition (VTD).
3. Titanium dioxide (TiO_2) is a wide band gap n-type semiconductor material, which has shown promise as a buffer layer for the Sb_2Se_3 solar cell.
4. As a part of TiO_2 treatment, air annealing after the deposition is a common applied procedure. However, the effect of vacuum annealing on structural and optoelectronic properties of the TiO_2 film and, consequently, TiO_2/Sb_2Se_3 solar cell is much less observed.

5. To improve the TiO_2/Sb_2Se_3 solar cell manufacturing procedure, optimal temperature and annealing environment for the TiO_2 buffer layer should be found.

According to this, the next aims could be stated for the following thesis:

1. To learn about the main principles of thin film solar cells, ultrasonic spray pyrolysis and close-spaced sublimation thin film deposition techniques, thin film characterization techniques from material (SEM, XRD, UV-VIS, XPS), and device (J-V, EQE) points of view.
2. To deposit sets of glass/FTO/TiO_2 thin films and glass/FTO/TiO_2/Sb_2Se_3/Au solar cells, implementing different post-deposition treatment procedures for the TiO_2 layer.
3. To analyze structural and optoelectronic properties of the TiO_2 thin films which experienced different post-deposition treatment procedures.
4. To investigate the effect of the TiO_2 post-deposition treatment procedures on the device performance of TiO_2/Sb_2Se_3 solar cells.

2. EXPERIMENTAL PART

During the study, two sets of samples were manufactured. The principal scheme of both sets is shown in figure 15. The processing sequence is described in figure 16.

Set 1 included TiO_2/FTO/glass stacks used for material characterization (such as XRD and UV-VIS). Set 2 included glass/FTO/TiO_2/Sb_2Se_3/Au solar cells with additional indium contacts, which operated as solar cells. Set 2 was used for solar cell characterization ((J-V, EQE).

Also, in parallel with set 1, TiO_2 was deposited onto glass without FTO. Under these conditions, titania remained amorphous.

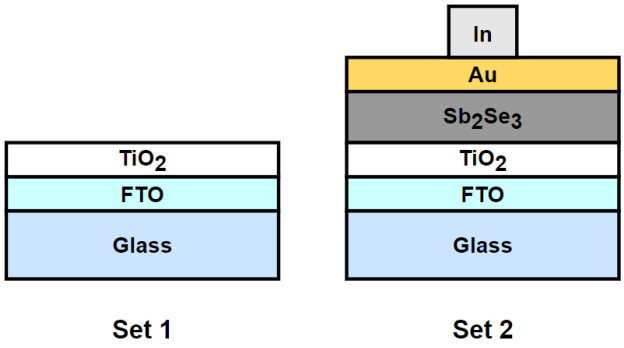

Fig. 15. Principal scheme of the sample sets.

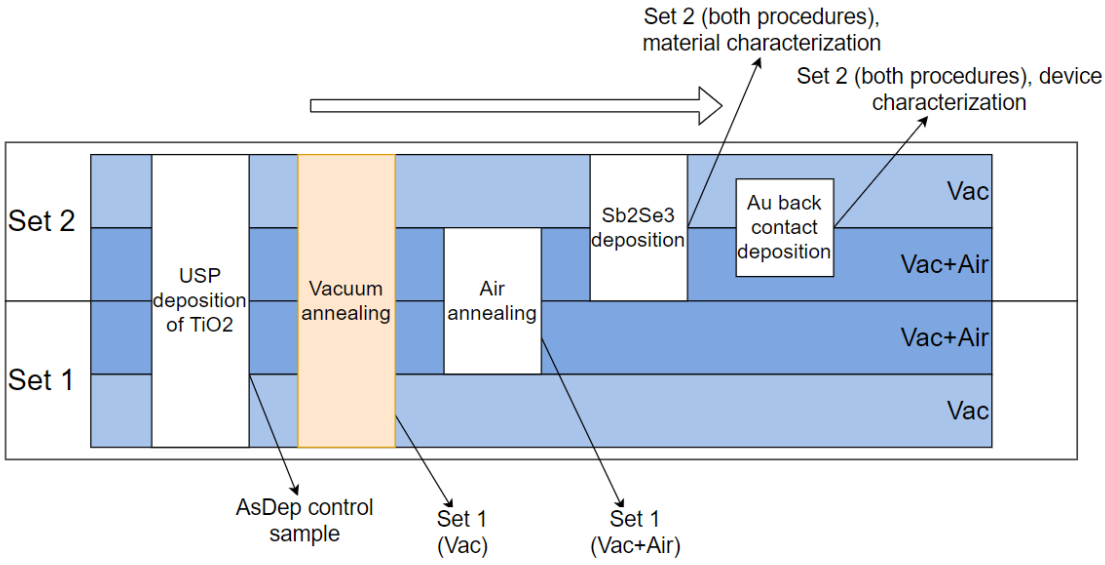

Fig. 16. Deposition sequence.

2.1. Fabrication of glass/FTO/TiO_2/Sb_2Se_3/Au solar cells

Glass/FTO substrate preparation

As a substrate, FTO-coated glass produced by Sigma-Aldrich Corporation was used. Glass thickness was 2.3 mm, declared surface resistivity ~7 Ω/sq.
The glass substrate was cut into squares (12x12 mm for set 1, 20x20 mm for set 2). Samples were marked by scribing their numbers on the glass side and then cleaned. The cleaning procedure consisted of dipping the samples in the solution (10 g $K_2Cr_2O_7$ + 10 mL H_20 + 100 mL H_2SO_4) for 1-3 hours, rinsing by deionized water, dipping in the boiling deionized water for 5-10 minutes, and then – drying in the flow of compressed or hot air.

TiO_2 deposition by ultrasonic spray pyrolysis (USP)

TiO_2 layer was deposited onto the FTO surface by USP. The substrate was heated up to 340 °C. Compressed air was used as a carrier gas. Precursor solution included titanium (IV) isopropoxide (TTIP) with the chemical formula of $C_{12}H_{28}O_4Ti$ and acetylacetone (AcAc) with the formula of $C_5H_8O_2$. The procedure was standardized to get the film thickness of 80-90 nm. The deposition was conducted in two steps. On the first step, TTIP and AcAc were dissolved in ethanol. 100 ml of solution consisted of 2.85 ml of TTIP, 4 ml of AcAc, and 93.15 ml of ethanol. 99 ml were used on the first deposition step, with a 7 ml/min flow rate of the carrier gas and 70 cycles of deposition. On average, the first step lasted for 24 min 57 sec and demanded 76 ml of solution. On the second step, one ml of the initial solution was dissolved into 250 ml of alcohol to get a diluted solution. 50 ml of this solution was used during one deposition. It was deposited with 3l/min flowrate and during 25 cycles. The average second step of deposition lasted for 8 min 51 sec and took 16 ml of diluted solution.
In the end, samples were cooled down for 5-10 minutes.

TiO_2/FTO/glass annealing

To research the combined influence of the vacuum annealing and the annealing in oxygen-rich conditions on TiO_2 film, two different annealing procedures were implemented, one-step and two-step.
The one-step procedure included only annealing in a vacuum at temperatures from 160 °C to 450 °C. For all samples, the temperature was increasing from the room temperature to the targeted one for 30 minutes and keeping for 30 minutes more, with subsequent cooling (20-30 minutes on average). Samples with TiO_2 annealed according to his procedure in the text are named VacX, where X is the temperature of vacuum annealing.

In the case of the two-step procedure, after vacuum annealing, samples were placed in the air furnace, where they were annealed at 450 °C for 30 minutes, with subsequent rapid cooling (10-15 minutes on average). Samples with TiO_2, which experienced a two-step annealing procedure, in-text are named as VacX+Air, where X is the temperature of vacuum annealing.

Vacuum annealing was conducted in a three-zone furnace Carbolite Gero EZS 1200. Air annealing was conducted in furnace T-40/600.

Annealing was the last step for set 1 preparation, whilst set 2 had two more steps.

Sb_2Se_3 deposition by close-spaced sublimation (CSS)

Antimony selenide absorber layer was deposited onto TiO_2/FTO/glass substrates by CSS. For all samples, Sb_2Se_3 absorber layers of 1.3-1.5 μm thickness were deposited by CSS (from 5N granular Sb_2Se_3 source material, provided by Sigma-Aldrich) at a source temperature of 490 °C keeping a deposition rate of ~1 μm min^{-1}.

Au back contact deposition by thermal evaporation

Golden back contacts were deposited onto glass/FTO/TiO_2/Sb_2Se_3 substrates, covered by mica masks. Areas of back contacts were 20-40 mm^2. After cooling, on the top of Au contacts and on the edges of FTO were soldered additional indium films to prevent scratching of the gold and ease the further measurements.

2.2. Material characterization

A Zeiss HR-SEM MERLIN scanning electron microscope (SEM) with the GEMINI II column was used to visualize crystal structure.

XRD characterization was carried on the Rigaku Ultima IV diffractometer by Cu Kα radiation (λ = 1. 54 Å, 40 kV, 40 mA). Rigaku PDXL software was used to analyze XRD data. Following data cards were used:

- JCPDS 01-089-0821 for Sb_2Se_3
- JCPDS 00-021-1272 for TiO_2
- JCPDS 01-077-0452 for FTO (SnO_2).

To maintain the Uv-VIS characterization in 300-1500 nm wavelength region, Jasco V-670 UV-Vis spectrophotometer with an integrating sphere was used. Using equations (2) and (3) from section 1.4.2, optical band gaps were calculated. Material characterization was conducted on the base of the Laboratory of Thin Film Chemical Technologies at Tallinn University of Technology.

XPS characterization was conducted on the hard X-ray photoelectron spectroscopy (HAXPES) analytical system, on the base of Competence Centre Photovoltaics Berlin (PVcomB), subdivision of Helmholtz Zentrum Berlin für Materialien und Energie (HZB).

2.3. Solar cell characterization

To measure the J-V characteristic of samples from set 2, AUTOLAB PGSTAT 30 and an Oriel class A solar simulator 91159A (100 mW cm-2, AM1.5) were used.

To conduct the EQE measurement for all samples from set 2, 300 W xenon lamp and an SPM-2 Carl Zeiss-Jena monochromator were used at 30 Hz. Solar cell characterization was conducted on the base of the Laboratory of Thin Film Chemical Technologies at Tallinn University of Technology.

3. RESULTS AND DISCUSSION

Chapter 3 presents the results of the research on structural, optical, and electrical properties of TiO_2 thin films and the performance of TiO_2/Sb_2Se_3 solar cells modified by PDTs.

In section 3.1, structural and optical properties of TiO_2 films treated according to different procedures and at different temperatures were investigated. Section 3.2 is devoted to the analysis of structural properties of Sb_2Se_3 films deposited atop TiO_2 from section 3.1 by CSS. Section 3.3. is focused on the electrical properties of resulting TiO_2/Sb_2Se_3 solar cells. Section 3.4 tells about the surface composition of TiO_2 film, studied via XPS.

3.1. Effect of annealing temperature and environment on TiO_2 thin film properties

In this thesis, the joint influence of two different annealing procedures was studied –vacuum annealing and consequent air annealing. Furthermore, TiO_2 buffer layers were prepared using either a two-step approach, which involved both vacuum and air annealing, or a single-step approach, where only vacuum annealing was applied. Considering that the two-step approach is subsequently labeled as "Vac+Air", whereas the single-step approach is labeled as "Vac". For the Vac procedure, glass/FTO/TiO_2 samples were annealed in a vacuum at temperatures between 160 °C and 450 °C for 30 minutes, without any further steps. In the case of the Vac+Air procedure, the vacuum annealing step (same with the Vac procedure) was always followed by air annealing at 450 °C for 30 minutes. A more detailed description of deposition and treatment procedures is included in Experimental section 2.1.
SEM, XRD, and UV-Vis techniques were used to analyze structural and optical properties of TiO_2, deposited on glass/FTO substrate and annealed according to Vac+Air and Vac procedures.
SEM study of glass/FTO/TiO_2 samples showed the dependence of TiO_2 film crystallinity upon vacuum annealing temperature. It can be seen from the top view SEM images in Fig. 17a and 17b. The cross-section for the sample, annealed according to Vac160+Air procedure, is shown in Fig. 17c. At low temperatures, grains form agglomerates, surrounded by a vast amount of amorphous phase. At 450 °C, larger grains have formed across the whole film.

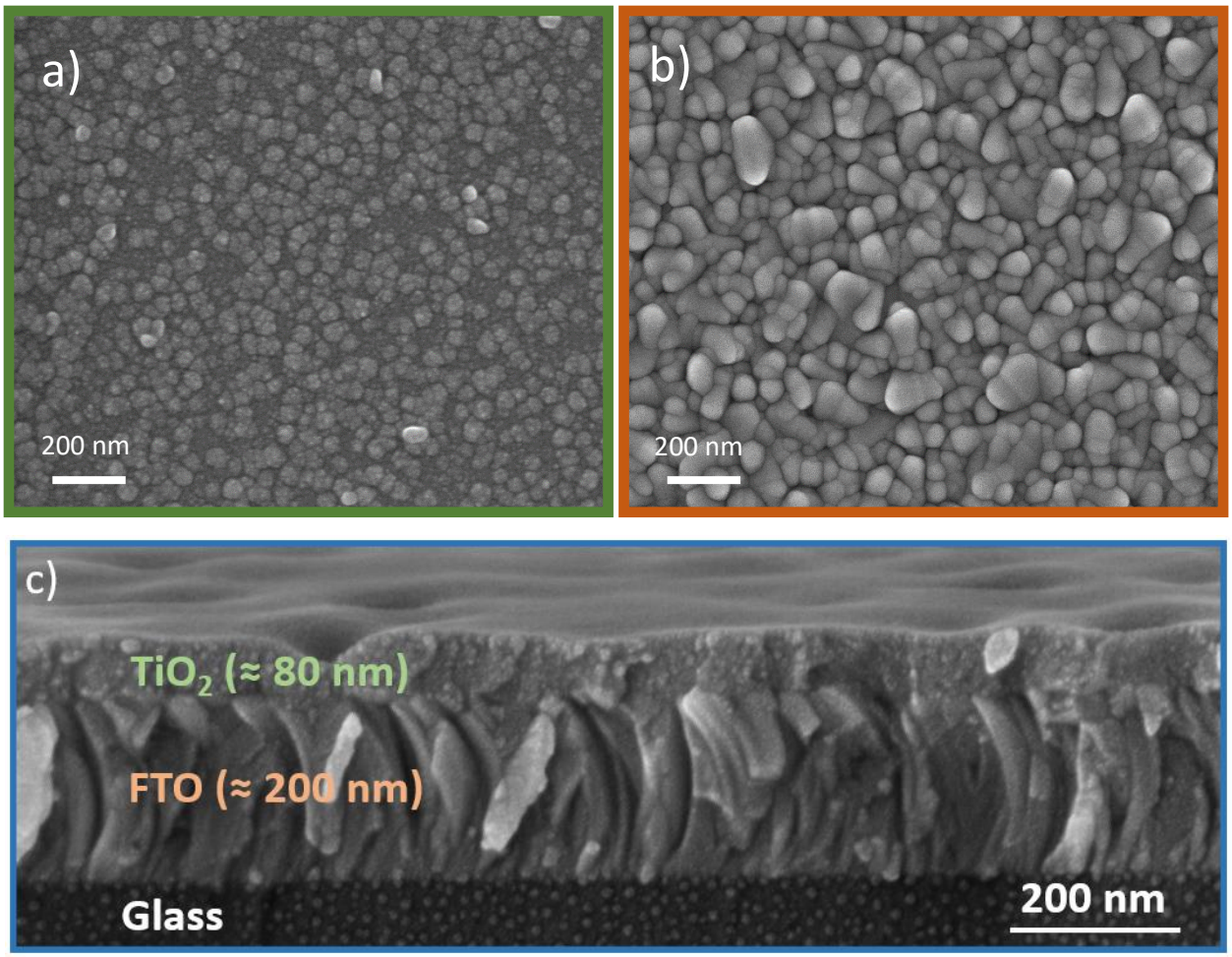

Fig. 17. Morphology of USP-deposited TiO_2 thin film, vacuum annealed at 160 °C(a) and 450 °C(b); cross-section of a typical glass/FTO/TiO_2 stack (c).

Figure 18 shows XRD patterns of glass/FTO/TiO_2, which were annealed according to Vac+Air (18.a) and Vac (18.b) procedures.

Given that the layer of TiO_2 was comparatively thin, 80–90 nm, the signal from FTO was stronger than from TiO_2. FTO peaks were cut to make TiO_2 peaks be more visible on the graph.

All the TiO_2 films deposited onto FTO/glass substrate were found to be polycrystalline. TiO_2 crystallized into the anatase phase (PDF card no. 00-021-1272). Two TiO_2-related peaks were found – (101) at 2θ=25.28° and (200) at 2θ =48.05°. These peaks have been previously reported for USP-deposited TiO_2 films.

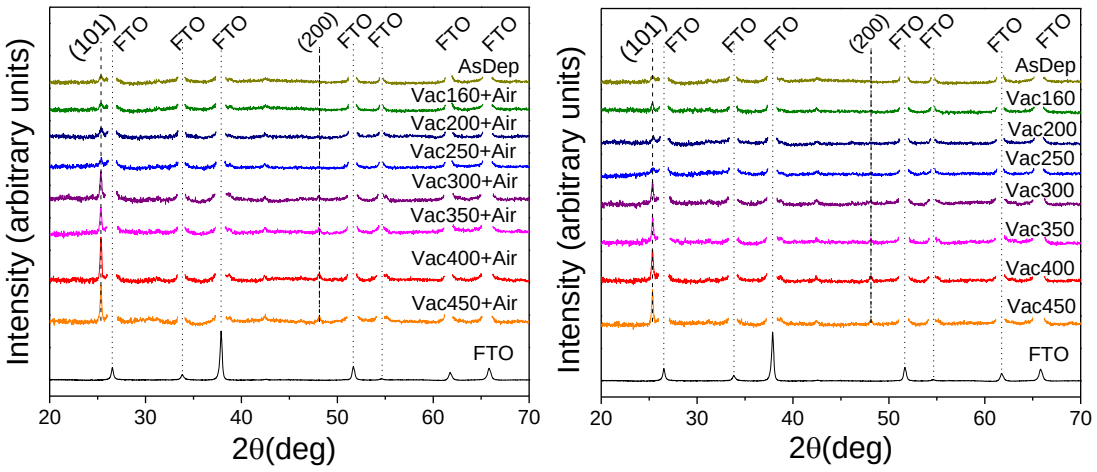

Fig.18. XRD patterns of TiO_2 films annealed in a vacuum at temperatures of 160 to 450 °C, a) with consequent air annealing (Vac+Air); b) without consequent air annealing (Vac).

At low temperatures below 300 °C, (101) the plane was mainly similar to the peak found in the AsDep sample. Also, a (200) peak was missing. Starting from 300 °C, intensities of both peaks are growing substantially, reaching the maximum at 400 °C (for Vac+Air procedure) and 450 ° C(for Vac procedure).

Intensity rise of the XRD peaks could be explained as a common effect seen after a) increase in the degree of crystallinity (which was observed by SEM) and b) increase in crystallite size. It can be concluded that at annealing temperatures below 300 °C, the influence of vacuum annealing on TiO_2 crystallization is neglectable. It was rather predictable – these temperatures are lower than 340 °C the temperature of USP deposition. However, for both procedures (Vac+Air and Vac), the leap in (101) peak intensity happens at 300 °C, which is still below the deposition temperature.

Crystallite size was increasing with temperature for both treatment procedures (Fig. 19). For the Vac+Air procedure (Fig. 19a), crystallites were ≈30 nm at low-T (120-250 °C) annealing and ≈ 50 nm at high-T (300-450 °C) annealing. In the case of the Vac procedure, this dependence vas more significant – after low-T vacuum treatments, crystallites were ≈ 20 nm large and after high-T treatment – 40-60 nm large, with the largest ones (61 nm) after the annealing at 450 °C (Fig. 19b).

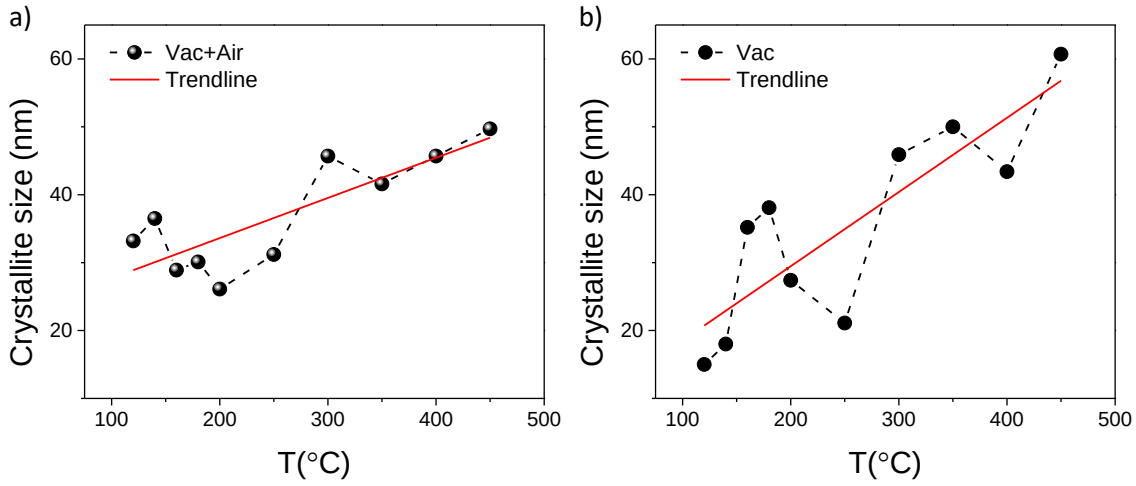

Fig.19. Crystallite sizes, extracted from TiO_2 XRD patterns, a) Vac+Air procedure; b) Vac procedure.

In the next step, UV-Vis was used to check any significant trends in band gap among the samples. Figure 20a shows the Tauc plot extracted from UV-Vis data for the Vac160+Air sample. A band gap of 3.3 eV was calculated. In the same way, band gaps were calculated for all samples from set 1, as shown in figure 20.b.

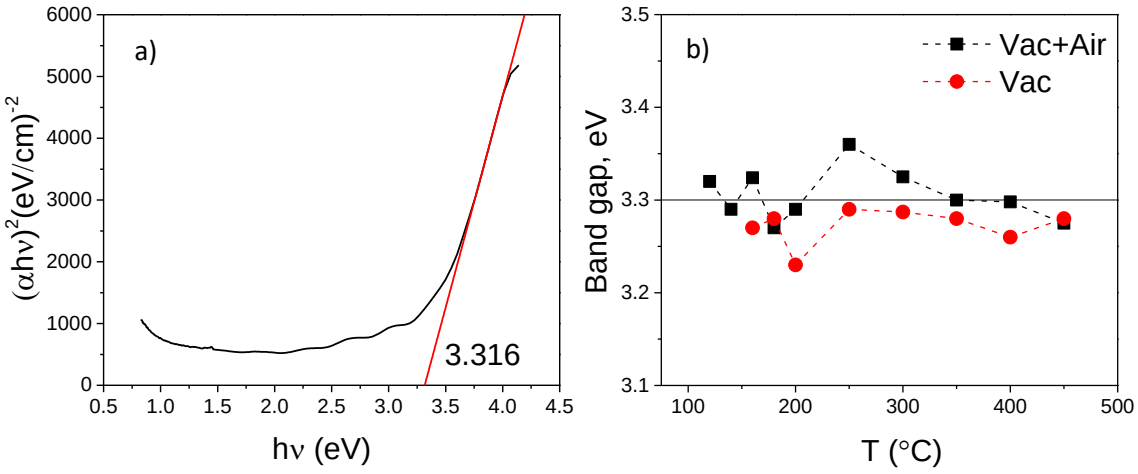

Fig.20. a) Tauc plot for Vac160+Air sample; b) Band gap of Vac+Air and Vac treated samples, calculated from UV-VIS data.

For all samples, the band gap lay between 3.2 and 3.4 eV. For all temperatures, except 180 °C, the band gap for Vac+Air treated samples was higher than for Vac treated samples. It could be that the influence of vacuum annealing temperature on the band gap is negligible.

To summarize - for both annealing procedures, the higher vacuum annealing temperature yields bigger crystal grains. XRD patterns that showed the presence of (101) and (200) together with the top-view SEM images revealed that TiO_2 films vacuum annealed at low temperatures include a more significant portion of amorphous TiO_2, as compared with the films annealed at higher temperatures. The temperature at which TiO_2 crystallized was at 300 °C. Otherwise, no significant differences between XRD patterns for Vac+Air and Vac procedures were found. According to UV-VIS, the band gap of TiO_2 varies slightly between 3.2–3.4 eV at temperatures of 160-450 °C.

3.2. Effect of TiO_2 annealing temperature and environment on grain growth of Sb_2Se_3 absorber

Section 3.2 reports on the effect of different TiO_2 post-deposition treatment procedures on Sb_2Se_3 film properties in glass/FTO/TiO_2/Sb_2Se_3 samples

Similar to the previous section, all samples were annealed according to two different procedures – Vac+Air and Vac. Vac+Air procedure was implemented for temperatures 160 – 450 °C, while Vac procedure was applied at temperatures 350–450 °C. Temperatures higher than 450 °C were not studied for the reason that TiO_2 undergoes a phase transition from anatase to rutile at 500-600 °C. Temperatures below the 350 °C were not studied for the single-step Vac annealing because annealing temperatures, which are already below the temperature of USP deposition, cannot possibly enable recrystallization of the TiO_2 film. Temperatures below 160 °C were not studied for two-step Vac+Air annealing because this has been already previously made [59].

XRD patterns were measured to investigate the potential influence of TiO_2 buffer layer Vac annealing temperature on Sb_2Se_3 absorber film structure. Figure 21 displays the XRD patterns of Sb_2Se_3film deposited by CSS onto TiO_2/FTO/glass substrates, which were previously annealed at temperatures 160-450 °C. To analyze the patterns, PDF JCPDS 01-089-0821 was used. Peaks, specific for orthorhombic Sb_2Se_3 were found at 2θ of 28.2°, 31.2°, 32.3°, 45.0°, 45.1°, 45.6°, which correspond to (211), (221), (301), (431), (501) and (002) planes, respectively.

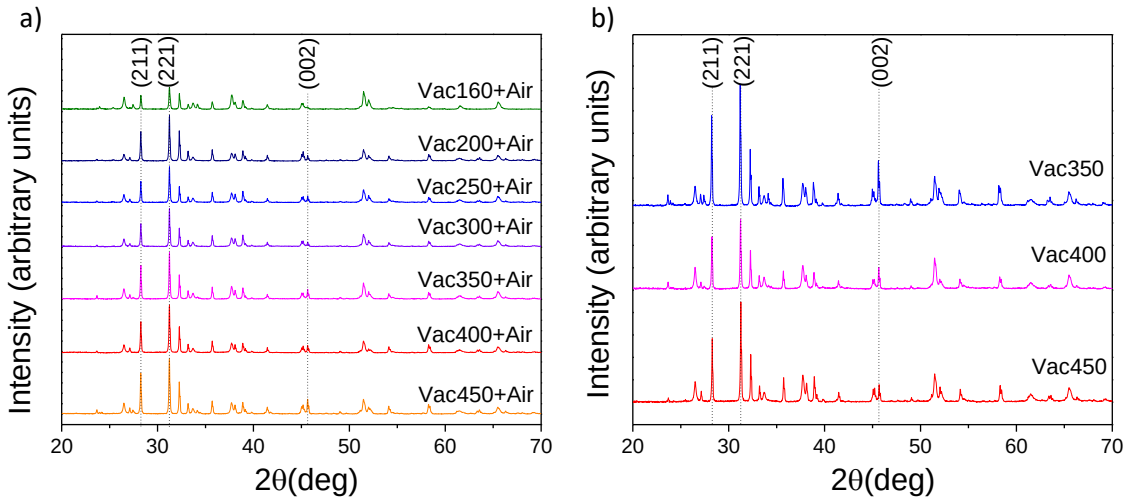

Fig. 21. XRD patterns of glass/FTO/TiO_2/Sb_2Se_3 films with TiO_2 substrate, treated a) according to Vac+Air procedure; b) according to Vac procedure.

All samples, both in Fig. 21a and 21b, show strongest peaks for the (211) and (221) peaks, which correspond to grains, which are inclined with respect to the surface normal.

To further examine the variation in crystal orientation, the texture coefficient (TC) was calculated using by Harris formula (eq. 9) [82]:

$$TC\ (hkl) = \frac{I(hkl)}{I_0(hkl)} \left[\frac{1}{N} \sum_{i=1}^{N} \frac{I(h_i k_i l_i)}{I_0(h_i k_i l_i)} \right]^{-1} \quad (9)$$

where I(hkl) is the intensity of given reflection found experimentally, and I_0(hkl) is the intensity obtained from the reference powder, N is the number of diffraction peaks considered in the calculations. Before the fitting, the background noise of the diffractogram was deconvoluted. The Lorentzian function was used for the peak integration.

TC analysis showed that TC values of the (211) and (211) planes increased with higher Vac annealing temperatures, as seen in Fig. 22b. A somewhat similar trend can be seen for Vac+Air annealed samples. It could mean that larger grains of TiO_2, as shown in Fig.19, improved Sb_2Se_3 crystal growth in 211 and 221 directions.

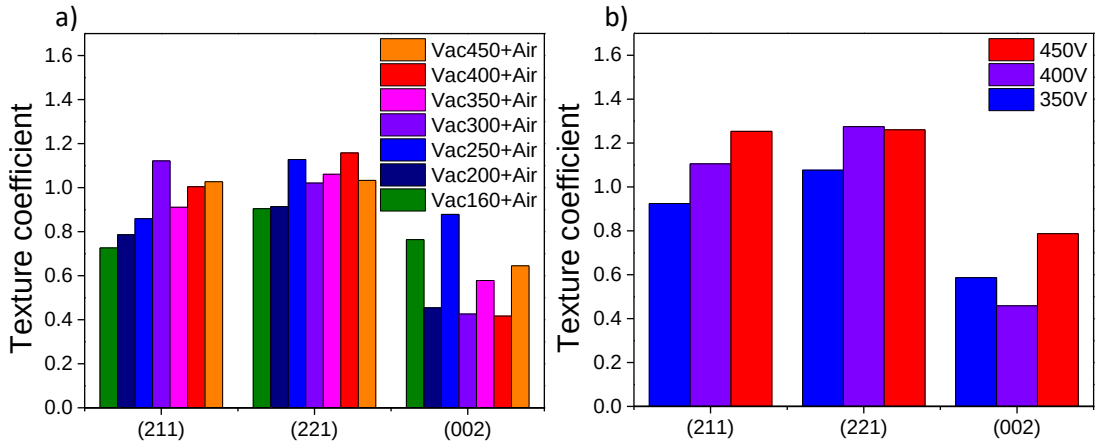

Fig. 22. Texture coefficients calculated from integrated intensity ratios for the dominant miller planes (211, 221, 002) of Sb_2Se_3 absorber.

The glass/FTO/TiO_2/Sb_2Se_3 film structures were studied by SEM. In Fig. 23a, it can be seen that Sb_2Se_3 forms large columnar grains on the top of the TiO_2 buffer layer. Fig. 23b shows the 90-95 nm layer of TiO_2 between FTO below and Sb_2Se_3 above it. Fig. 23c shows the top view of Sb_2Se_3 film, which is rather homogenous and includes very few voids in it.

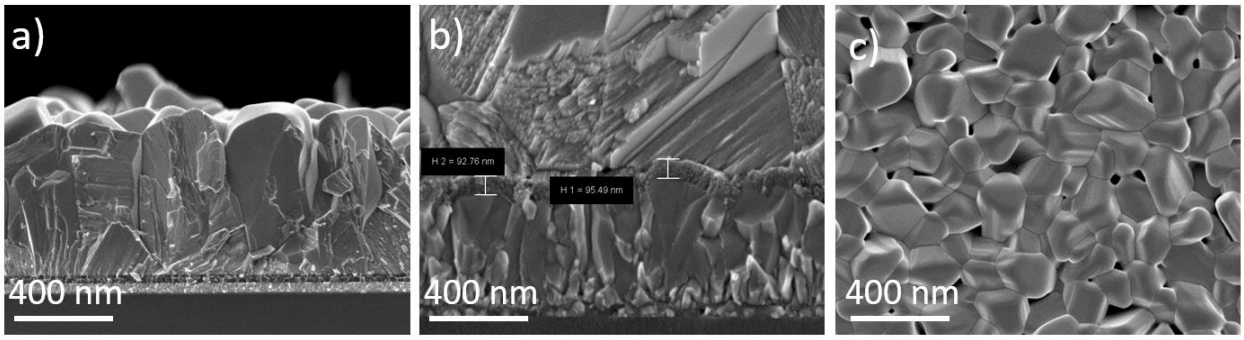

Fig. 23. SEM image of the Vac160+Air annealed glass/FTO/TiO_2 substrate with CSS-deposited Sb_2Se_3: cross-section focused on the Sb_2Se_3 grains (a), cross-section focused on 92-95-nm thick TiO_2 layer (b), top view (c)

It could be assumed that larger grains of buffer layer provide more suitable conditions for growing Sb_2Se_3 film.

3.3. Effect of TiO_2 annealing temperature and environment on electrical characteristics of glass/FTO/TiO_2/Sb_2Se_3/Au solar cells

Section 3.3. is devoted to the investigation into the effect of different TiO_2 buffer layer vacuum annealing temperatures on the glass/FTO/TiO_2/Sb_2Se_3/Au solar cell performance.

Figure 24a shows current-voltage (J-V) curves for solar cells with Vac+Air annealed substrates, whereas Fig. 24b – J-V characteristics of three solar cells with Vac annealed substrates. In both figures, a solar cell with air annealed substrate was added for reference. Table 2 shows the main photovoltaic parameters of the samples. J-V curves in Fig. 24a shows that the solar cell with a the efficiency of 3.96%, made by Vac160+Air procedure, is the most efficient device among the studied ones. It is followed by the device with a buffer layer, annealed at 120 °C, with 3.59% efficiency.

As seen in Table 2, solar cells deposited according to Vac+Air show higher V_{oc}, J_{sc}, FF, and efficiency. All characteristics of the Vac160+Air are lower than the characteristics of the record cell [41], except for the J_{sc} (24.5 mA/cm^2).

J-V curves show different trends for Vac+Air and Vac procedures. In the case of Vac+Air, as seen in Fig. 24a, Vac450+Air and Vac350+Air solar cells perform clearly worse than Vac160+Air and Vac250+Air samples and are similar to the reference solar cell.

Results show that the lower is the vacuum annealing temperature, the better is the device performance. In the case of Vac annealing, as shown in Fig. 24b, all solar cells performed worse than the reference solar cell. Vac400 and Vac450 had similar J_{sc} and V_{oc}, while Vac350 shows a drop in J_{sc} to 11.6 mA/cm^2 and an increase of V_{oc} to 242.67 mV. Vac350 produced an efficiency of 0.83%, which is the lowest among all samples. Most importantly, these results indicate the necessity of air annealing for optimal TiO_2 performance in a TiO_2/Sb_2Se_3 solar cell.

External Quantum Efficiency (EQE) of solar cells with different annealing procedures are given in Fig. 25 – and EQE data support the findings above. Vac160+Air device shows the highest spectral response from 350 to 900 nm, which then declines sharply.

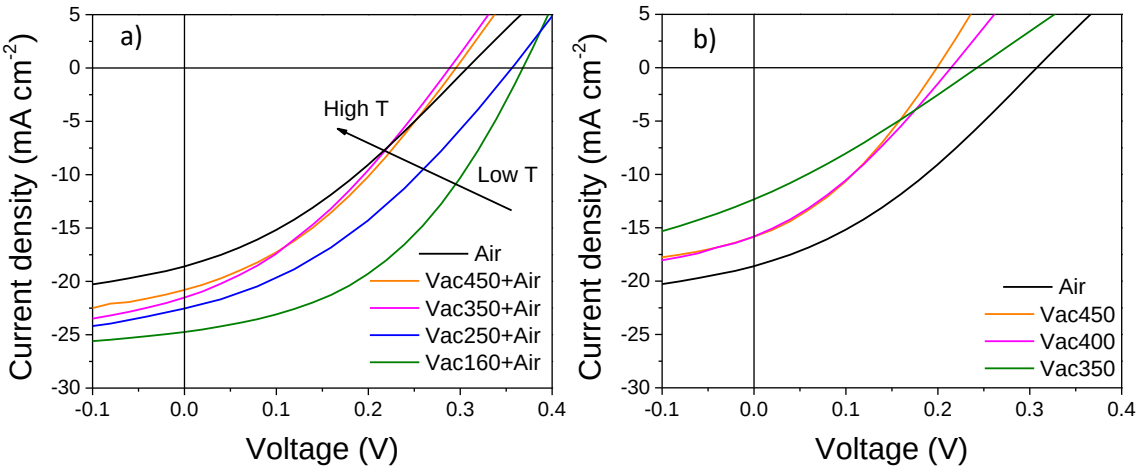

Fig. 24. J-V characteristics of glass/FTO/TiO_2/Sb_2Se_3/Au solar cells with buffer layer treated a) according to Vac+Air procedure; b) according to Vac procedure.

Table 2. Photovoltaic parameters of glass/FTO/TiO_2/Sb_2Se_3/Au solar cells with a buffer layer treated according to Vac, Air, and Vac+Air procedures.

T_{vac} (°C)	Procedure	V_{oc}, mV	s, mA/cm^2	FF, %	Eff, %
No vac	Air	300.4	18.1	34	1.89
450	Vac+Air	293.02	17.7	34.6	1.79
	Vac	199.07	15.2	35.3	1.52
400	Vac+Air	296.58	17.7	31.4	1.64
	Vac	214.36	15.1	33.4	1.54
350	Vac+Air	288.53	20.9	34.8	2.1
	Vac	242.67	11.6	29.8	0.83
300	Vac+Air	339.03	22.2	39.7	2.95
250	Vac+Air	356.17	21.7	37	2.85
200	Vac+Air	360.03	23	39.5	3.3
160	**Vac+Air**	**368.05**	**24.5**	**43.9**	**3.96**
120	Vac+Air	354.21	24.4	41.5	3.59

Vac450+Air solar cells have a higher EQE response in the 650-900 nm region than in the 400-650 region. At 400 °C, the shape of the curve looks well-balanced, but the EQE is weaker comparing with lower temperatures. At 350 °C and lower temperatures until 160 °C, EQE is constantly rising for all intervals, and for all samples in this range of temperatures left side of

the graph is higher than the right one. After the peak EQE values at 160 °C, EQE drops down to 120 °C, indicating peak values between 120 °C and 200 °C.

For the Vac procedure, only three samples were examined. For all temperatures, EQE was lower compared with their counterparts treated according to the Vac+Air procedure. The shape of 450 °C is close to its shape for Vac+Air. At Vac 400 °C, the highest EQE for almost all spectrum regions is gained, close to the Vac+Air 400 °C sample. However, at a lower temperature (350 °C), EQE is not rising, like in the previous set, but drops down.

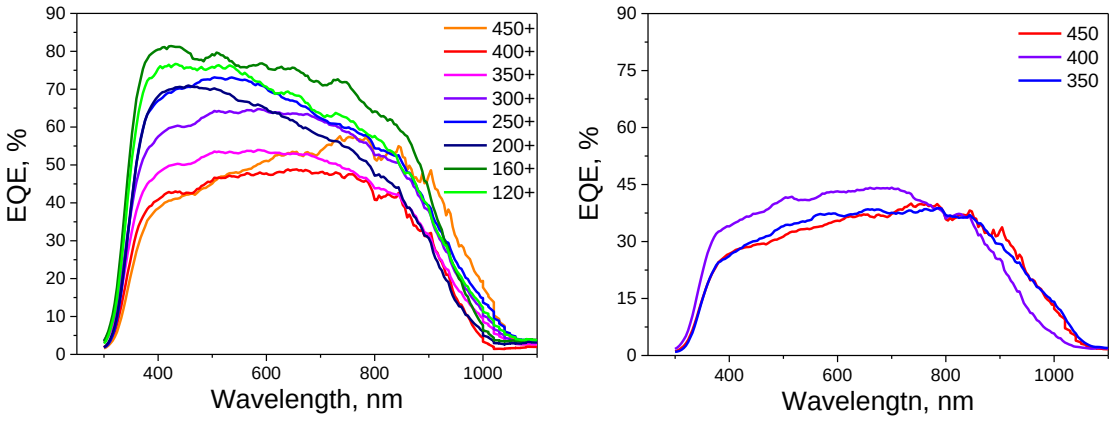

Fig. 25. Normalized EQE of glass/FTO/TiO_2/Sb_2Se_3/Au solar cells with a buffer layer, treated a) according to Vac+Air procedure; b) according to Vac procedure.

At this step, it was clearly visible that both the temperature of vacuum annealing and subsequent air annealing actively influence the efficiency of the solar cell. Previous studies have attributed the increase of solar cell efficiency to the reduction of carbon content in the TiO_2 films [9]. Since the results presented in this thesis clearly support a two-step procedure, this may well be additional proof about the role of carbon in the TiO_2/Sb_2Se_3 device performance. However, vacuum annealing at higher temperatures looks somewhat counterintuitive – the higher was the vacuum annealing temperature, the lower was the cell efficiency. Therefore, the following assumptions about the differences in annealing in an oxygen-rich atmosphere and a vacuum were made.

The role of oxygen is somewhat unclear in terms of TiO_2/Sb_2Se_3 p-n heterojunction. TiO_2 is an n-type semiconductor, which should have more carriers to perform its function. It implies that it should have more oxygen vacancies – and prior research was focused on increasing their concentration via TiO_2 annealing in oxygen-poor conditions (vacuum, N, Ar) [83]. However, when samples were exposed to air (even at room temperature), the concentration of oxygen vacancies was rapidly decreasing.

It can be implied that during air annealing, oxygen is actively incorporated into TiO_2 film. The degree and rate of liquid-phase sintering are inversely proportional to the dimensions of the initial TiO_2 particles. Thus, TiO_2 films annealed at low substrate temperatures have a highly dispersed structure with smaller grains and smaller crystallite sizes (seen in section 3.1), and high surface energies [13]. Therefore, these grains are more active in terms of recrystallization by mass transport through the air atmosphere, compared with larger grains. At the same step, oxygen is actively diffusing into the TiO_2 structure, leading to a significant decrease in the number of oxygen vacancies in the film. It should decrease the efficiency of the cell – but it instead increases roughly two times.
One of the likely answers could be that oxygen acts as a passivator of Sb_2Se_3 grain boundaries during the Sb_2Se_3 deposition – in the same manner as chlorine and oxygen act for CdTe [84][85]. It neutralizes their dangling bonds and reduces the number of potent trap states in the Sb_2Se_3 area of the p-n junction. The influence of passivation could overcome the negative effect of oxygen on the number of carriers. The even higher efficiency can probably be shown by the solar cells with passivated Sb_2Se_3 grain boundaries, but without decreasing the number of oxygen vacancies.

To summarize, despite the gradual improvement of the strusture in both TiO_2 and Sb_2Se_3 layers with temperature, the electrical characteristics of the devices have shown opposite trends. At high temperatures, cells have shown low efficiency (1-2%), and the most efficient sample was made by Vac160+Air procedure. Vac samples have shown far lower efficiency, comparing with their Vac+Air counterparts. Also, Vac samples were found less efficient than Air-annealed control sample. It was a rather counterintuitive result – based on parts 3.1. and 3.2. it was possible to suppose that after a low-temperature vacuum, TiO_2 will show rather bad electrical properties. Also, no substantial difference between Vac and Vac+Air treated samples was observed on previous steps. The role of air annealing was associated with oxygen incorporation into TiO_2 structure and temperature dependence of efficiency – with the incorporation into the films with different structural and structural properties. The possibility of a passivating effect of additional oxygen from TiO_2 film on Sb_2Se_3 grain boundaries was implied. Also, the prior hypothesis that the role of vacuum annealing could be explained by the remains of organic on the surface of TiO_2, strongly influenced by the annealing procedure, received additional proofs. To check both the concepts of carbon residuals and incorporated oxygen in variously treated TiO_2, XPS measurement was involved.

XPS analysis has shown the presence of carbon in the surface layer of TiO_2 film. The concentration of organic residuals was low in terms of the whole film, and thus it was below the detection limit of other techniques. In literature is believed that at the stage of air

treatment, all the organic residuals of Ti complex together with hydrogen, oxygen, and carbon are fully oxidized and removed as vapors of H_2O and CO, CO_2 gas. Nevertheless, few recent studies from the photocatalysis field have shown the presence of carbon species in TiO_2 films (deposited via spray pyrolysis and spin coating) after air annealing at temperatures higher than 500 °C and even after additional ultraviolet treatment [86][87]. In this study, they were found in all samples, but their concentration was different.

Four samples (untreated one (as-dep), Vac160, Air, and Vac160+Air) were analyzed using the XPS technique. The generalized XPS pattern for all examined samples can be seen in Fig. 26a. Zoomed picture of carbon (C1s) peak is shown in Fig. 26b. The intensity of carbon peak was found different for all samples. The emission line at 285.0 eV is attributed to carbon species. It can be seen that as-deposited TiO_2 films contain the highest concentration of carbon species. Thermal annealing in a vacuum at 160 °C decreases the concentration of carbon.

Nevertheless, a significant amount of organic remains in the films can be located at the grain boundaries and in the lattice of TiO_2 layers. The concentration of carbon in the air-annealed film is even lower, and the lowest one is observed in the Vac+Air sample. According to the measured XPS patterns, data about the atomic percentage of different compounds were calculated in table 3 (Fig. 26c). The concentration of carbon is steadily decreasing after every step post-deposition treatment, with the highest for the as-dep sample (37.2 at%) and lowest for the Vac+Air sample (16.3 at%). Also, the concentration of oxygen in the case of the Vac+Air sample was found much higher, comparing with the Vac sample (63.5% vs. 52.5%). It fits the priorly given hypothesis from section 3.3.

Table 3. The concentration of C, N, O, Sn, and Ti in four observed samples.

Sample	as-dep	Vac	Air	Vac+Air
	at%	at%	at%	at%
C1s	**37.2**	**36**	**28.2**	**16.3**
N1s	0.7	0.6	0.6	1.5
O1s	**47.2**	**47.6**	**52.5**	**63.5**
$Sn3d_{5/2}$	4.2	0	0	0
$Ti2p_{3/2}$	10.7	15.9	18.7	18.8

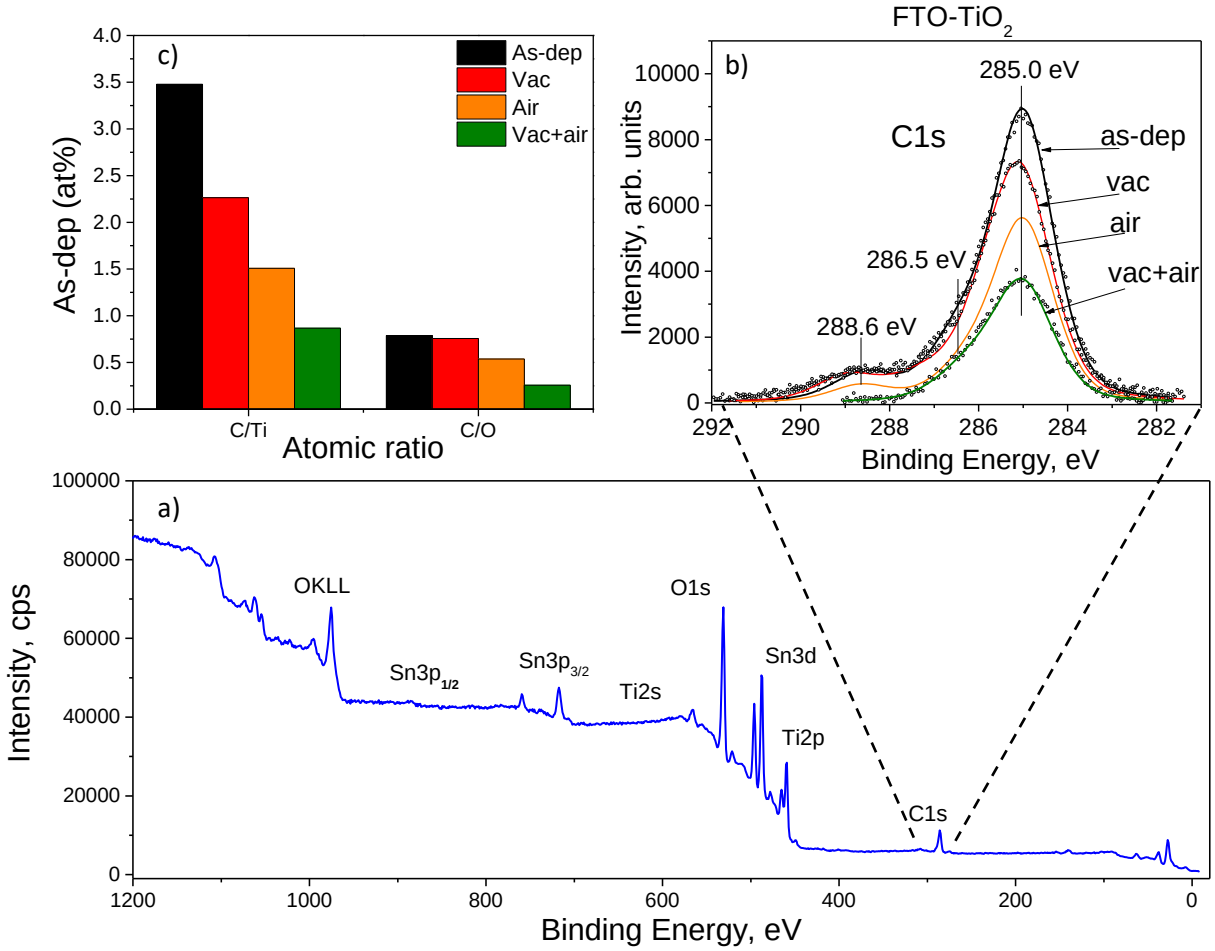

Fig. 26. XPS pattern for FTO/TiO_2 film (a); with zoomed C1s peak with separated patterns for as-deposited sample (as-dep), annealed in vacuum at 160 °C (vac), annealed in air at 450 °C (air), and annealed both in vacuum at 160 °C and in the air at 450 °C (vac+air) (b); calculated atomic ratios C/Ti and C/O for all four samples (c).

The hypothesis from [9] about the carbon content was fully approved by XPS measurement. The significant difference in carbon content can be the reason for the previously observed difference in the efficiency between Vac, Air, and Vac+Air samples. It can be supposed that organic residuals were originating from USP precursor solution act as defects at the TiO_2/Sb_2Se_3 interface, which reduces the performance of solar cells. At every further treatment step, the amount of this organic is decreasing. Low-temperature (160 °C) vacuum annealing has lower efficiency in carbon out-diffusion comparing with high-temperature (450 °C) air annealing. The combination of these two procedures (Vac+Air) has shown the best result both in terms of carbon content and solar cell efficiency.

It can be assumed that the efficiency of organic out-diffusion in a vacuum increases with the temperature. However, starting from 160 °C, it is suppressed by the growing crystallinity of the film and consequent decreasing of the amount of the incorporated oxygen. According to the above-described hypothesis, it decreases the measure of the further passivation of the Sb_2Se_3 grain boundaries and consequently decreases the efficiency of the cell. So, the Vac160+Air procedure seems to be not optimal in terms of buffer layer crystallinity but optimal in terms of carbon and oxygen, which is more influential in terms of device efficiency.

CONCLUSIONS

This thesis focused on the post-deposition treatment of the USP-deposited TiO_2 buffer layer for TiO_2/Sb_2Se_3 solar cells. TiO_2 buffer layers were annealed using either a two-step approach, which involved both vacuum and air annealing, or a single-step approach, where only vacuum annealing was applied. Vacuum annealing was applied at temperatures ranging from 160 °C to 450 °C, whereas air annealing was always carried out at 450 °C. PDT conditions were varied to study their effect on (1) the structural and optoelectronic properties of the TiO_2 films by SEM, XRD, UV-vis spectroscopy, and XPS (2) the structural properties of Sb_2Se_3 grown on top of TiO_2 buffer films by SEM and XRD and (3) the performance of TiO_2/Sb_2Se_3 solar cell by J-V curve and EQE measurements.

TiO_2 thin films revealed that crystallite size depended upon the temperature of vacuum annealing. The higher was the temperature, the larger the crystallites were (an increase from 20-30 to 50-60 nm), and the more homogeneous films were observed. No significant structural difference was noted between Vac and Vac+Air treated samples. Nevertheless, Vac+Air samples showed a bit larger (by 0.05 eV) optical band gap. Structural properties of Sb_2Se_3 film, deposited atop of differently annealed glass/FTO/TiO_2, have shown a weak trend of having more oriented towards (221) and (211) directions crystallites at higher temperatures. Again, no significant difference between Vac and Vac+Air was recognized. Both the size of grains in the buffer layer and more prominent columnar orientation of absorber layer crystallites are rather positive signs for a photovoltaic device, so barely based on sections 3.1 and 3.2, it was possible to say that high-temperature vacuum annealing improves the properties of TiO_2 buffer layer for Sb_2Se_3-based solar cell. However, at the step of photovoltaic efficiency, the picture was totally opposite. All electric parameters of Vac solar cells (0.83%-1.54%) were overwhelmed by Vac+Air counterparts (1.79%-3.96%), and the highest efficiency (3.96%) was shown by the Vac160+Air sample, which was annealed in vacuum at almost the lowest temperature.

Therefore, two significant trends were revealed: high temperature of vacuum annealing of TiO_2 corresponds to the lower efficiency of the solar cell; air annealing, applied after vacuum annealing, increases the efficiency of the solar cell. These trends were associated with the influence of oxygen incorporation during the air annealing (could be recognized as an oxygen-rich environment) and the efficiency of this incorporation. A less crystalline film can absorb more oxygen at the step of air annealing. Low-temperature annealed TiO_2 remained less crystalline and, therefore, went through more significant recrystallization during air annealing. So, low-temperature vacuum annealing provided the most suitable conditions for consequent

oxygen incorporation. XPS measurement has shown that the surface of all glass/FTO/TiO_2 samples included harmful remains of carbon compounds used in USP deposition. With every following step of post-deposition treatment, their content decreased, which could be a reason for the higher efficiency of Vac+Air samples.

Altogether, the research highlighted the importance of the post-deposition TiO_2 treatment. It clarified the role of different PDT steps in terms of carbon expulsion and oxygen implantation, which were both shown a significant impact on the TiO_2/Sb_2Se_3 solar cell performance.

REFERENCES

[1] "Basic Photovoltaic Principles and Methods," 1982. [Online]. Available: https://www.nrel.gov/docs/legosti/old/1448.pdf.

[2] I. Renewable and E. Agency, *Renewable capacity statistics 2021 Statistiques de capacité renouvelable 2021 Estadísticas de capacidad renovable 2021*. 2021.

[3] "Renewable energy | Energy economics | Home." https://www.bp.com/en/global/corporate/energy-economics/statistical-review-of-world-energy/renewable-energy.html#solar-energy (accessed Apr. 11, 2021).

[4] "GOAL 7: Affordable and clean energy | UNEP - UN Environment Programme." https://www.unep.org/explore-topics/sustainable-development-goals/why-do-sustainable-development-goals-matter/goal-7 (accessed Apr. 11, 2021).

[5] "Global energy transformation: A roadmap to 2050 (2019 edition)," */publications/2019/Apr/Global-energy-transformation-A-roadmap-to-2050-2019Edition*, Accessed: Apr. 11, 2021. [Online]. Available: /publications/2019/Apr/Global-energy-transformation-A-roadmap-to-2050-2019Edition.

[6] "Global Thin-Film Module Market (2020 to 2025) - Players Include United Solar Ovonic, TS Solar and NanoPV Solar Among Others." https://www.globenewswire.com/news-release/2020/11/27/2135191/0/en/Global-Thin-Film-Module-Market-2020-to-2025-Players-Include-United-Solar-Ovonic-TS-Solar-and-NanoPV-Solar-Among-Others.html (accessed Apr. 11, 2021).

[7] "Best Research-Cell Efficiencies." https://www.nrel.gov/pv/assets/pdfs/best-research-cell-efficiencies.20200104.pdf (accessed Apr. 11, 2021).

[8] K. A. W. Horowitz, R. Fu, X. Sun, T. Silverman, M. Woodhouse, and M. A. Alam, "An Analysis of the Cost and Performance of Photovoltaic Systems as a Function of Module Area," 2017. Accessed: Apr. 12, 2021. [Online]. Available: www.nrel.gov/publications.

[9] N. Spalatu *et al.*, "Screening and optimization of processing temperature for Sb2Se3 thin film growth protocol: Interrelation between grain structure, interface intermixing and solar cell performance," *Sol. Energy Mater. Sol. Cells*, vol. 225, p. 111045, Jun. 2021, doi: 10.1016/j.solmat.2021.111045.

[10] "Power for the World: The Emergence of Electricity from the Sun - Wolfgang Palz - Google Книги." https://books.google.ee/books?id=sEINA3tyLUAC&q=%22Power+for+the+World+-+The+Emergence+of+Electricity+from+the+Sun%22&redir_esc=y#v=snippet&q=%22Power for the World - The Emergence of Electricity from the Sun%22&f=false (accessed Feb. 03, 2021).

[11] J. L. Gray, *The Physics of the Solar Cell*. 2011.

[12] R. Alicki, D. Gelbwaser-Klimovsky, and A. Jenkins, "A thermodynamic cycle for the solar cell," *Ann. Phys. (N. Y).*, vol. 378, pp. 71–87, Mar. 2017, doi: 10.1016/j.aop.2017.01.003.

[13] N. Spalatu, *Development of CdTe absorber layer for thin-film solar cells*. Tallinn: TUT Press, 2017.

[14] N. Spalatu *et al.*, "Properties of the CdCl2 air-annealed CSS CdTe thin films," in *Energy Procedia*, 2014, vol. 44, pp. 85–95, doi: 10.1016/j.egypro.2013.12.013.

[15] X. Wen *et al.*, "Vapor transport deposition of antimony selenide thin film solar cells with 7.6% efficiency," *Nat. Commun.*, vol. 9, no. 1, pp. 1–10, Dec. 2018, doi: 10.1038/s41467-018-04634-6.

[16] L. J. Phillips *et al.*, "Current Enhancement via a TiO 2 Window Layer for CSS Sb 2 Se 3 Solar Cells: Performance Limits and High V oc," *IEEE J. Photovoltaics*, vol. 9, no. 2, pp. 544–551, 2019, doi: 10.1109/JPHOTOV.2018.2885836.

[17] "Data – Emerging PV." https://emerging-pv.org/data/ (accessed May 18, 2021).

[18] C.B.Honsberg and S.G.Bowden, "Absorption Coefficient | PVEducation." https://www.pveducation.org/pvcdrom/pn-junctions/absorption-coefficient (accessed May 18, 2021).

[19] M. A. Green, E. D. Dunlop, J. Hohl-Ebinger, M. Yoshita, N. Kopidakis, and X. Hao, "Solar cell efficiency tables (version 56)," *Prog. Photovoltaics Res. Appl.*, vol. 28, no. 7, pp. 629–638, Jul. 2020, doi: 10.1002/pip.3303.

[20] R. Kondrotas, C. Chen, and J. Tang, "Sb2S3 Solar Cells," *Joule*, vol. 2, no. 5. Cell Press, pp. 857–878, May 16, 2018, doi: 10.1016/j.joule.2018.04.003.

[21] F. Ise, "Photovoltaics Report." Accessed: May 18, 2021. [Online]. Available: www.ise.fraunhofer.de.

[22] S. Khalid, M. Sultan, E. Ahmed, and W. Ahmed, "Third-generation solar cells," in *Emerging Nanotechnologies for Renewable Energy*, Elsevier, 2021, pp. 3–35.

[23] T. M. Razykov, A. X. Shukurov, O. K. Atabayev, K. M. Kuchkarov, B. Ergashev, and A. A. Mavlonov, "Growth and characterization of Sb2Se3 thin films for solar cells," *Sol. Energy*, vol. 173, pp. 225–228, Oct. 2018, doi: 10.1016/j.solener.2018.07.082.

[24] Z. Li *et al.*, "9.2%-efficient core-shell structured antimony selenide nanorod array solar cells," *Nat. Commun.*, vol. 10, no. 1, pp. 1–9, Dec. 2019, doi: 10.1038/s41467-018-07903-6.

[25] X. Wen *et al.*, "Vapor transport deposition of antimony selenide thin film solar cells with 7.6% efficiency," *Nat. Commun.*, vol. 9, no. 1, pp. 1–10, 2018, doi: 10.1038/s41467-018-04634-6.

[26] X. Liu *et al.*, "Thermal evaporation and characterization of Sb2Se3 thin film for substrate Sb2Se3/CdS solar cells," *ACS Appl. Mater. Interfaces*, vol. 6, no. 13, pp. 10687–10695, 2014, doi: 10.1021/am502427s.

[27] G. Ghosh, "The sb-se (antimony-selenium) system," *J. Phase Equilibria*, vol. 14, no. 6, pp. 753–763, 1993, doi: 10.1007/BF02667889.

[28] Z. Li *et al.*, "Sb2Se3 thin film solar cells in substrate configuration and the back contact selenization," *Sol. Energy Mater. Sol. Cells*, vol. 161, pp. 190–196, Mar. 2017, doi: 10.1016/j.solmat.2016.11.033.

[29] L. Guo *et al.*, "Tunable Quasi-One-Dimensional Ribbon Enhanced Light Absorption in Sb2Se3 Thin-film Solar Cells Grown by Close-Space Sublimation," *Sol. RRL*, 2018, doi: 10.1002/solr.201800128.

[30] N. Spalatu *et al.*, "Effect of CdCl2annealing treatment on structural and optoelectronic

properties of close spaced sublimation CdTe/CdS thin film solar cells vs deposition conditions," in *Thin Solid Films*, May 2015, vol. 582, pp. 128–133, doi: 10.1016/j.tsf.2014.11.066.

[31] S. Polivtseva, N. Spalatu, A. Abdalla, O. Volobujeva, J. Hiie, and S. Bereznev, "Pulsed Laser Deposition of Zn(O,Se) Layers for Optoelectronic Application," *ACS Appl. Energy Mater.*, vol. 1, no. 11, pp. 6505–6512, Nov. 2018, doi: 10.1021/acsaem.8b01431.

[32] L. Yu and A. Zunger, "Identification of Potential Photovoltaic Absorbers Based on First-Principles Spectroscopic Screening of Materials," 2012, doi: 10.1103/PhysRevLett.108.068701.

[33] "ANTIMONY (III) SELENIDE | 1315-05-5." https://www.chemicalbook.com/ChemicalProductProperty_EN_CB2124719.htm (accessed Feb. 03, 2021).

[34] Y. Zhou *et al.*, "Thin-film Sb2Se3 photovoltaics with oriented one-dimensional ribbons and benign grain boundaries," *Nat. Photonics*, vol. 9, no. 6, pp. 409–415, Jun. 2015, doi: 10.1038/nphoton.2015.78.

[35] Jako S. Eensalu *et al.*, "Uniform Sb2S3 optical coatings by chemical spray method," *Beilstein J. Nanotechnol.*, vol. 10, no. 1, pp. 198–210, 2019, doi: 10.3762/bjnano.10.18.

[36] S. Messina, M. T. S. Nair, and P. K. Nair, "Antimony Selenide Absorber Thin Films in All-Chemically Deposited Solar Cells," 2009, doi: 10.1149/1.3089358.

[37] Y. C. Choi *et al.*, "Sb2Se3-sensitized inorganic-organic-heterojunction solar cells fabricated using a single-source precursor," *Angew. Chemie - Int. Ed.*, vol. 53, no. 5, pp. 1329–1333, Jan. 2014, doi: 10.1002/anie.201308331.

[38] O. S. Hutter, L. J. Phillips, K. Durose, and J. D. Major, "6.6% efficient antimony selenide solar cells using grain structure control and an organic contact layer," *Sol. Energy Mater. Sol. Cells*, vol. 188, pp. 177–181, Dec. 2018, doi: 10.1016/j.solmat.2018.09.004.

[39] T. D. C. Hobson *et al.*, "Isotype Heterojunction Solar Cells Using n-Type Sb2Se3 Thin Films," *Chem. Mater.*, 2020, doi: 10.1021/acs.chemmater.0c00223.

[40] R. Tang *et al.*, "Hydrothermal deposition of antimony selenosulfide thin films enables solar cells with 10% efficiency," *Nat. Energy*, vol. 5, no. 8, pp. 587–595, Aug. 2020, doi: 10.1038/s41560-020-0652-3.

[41] X. Wang *et al.*, "Manipulating the Electrical Properties of $Sb_2(S,Se)_3$ Film for High-Efficiency Solar Cell," *Adv. Energy Mater.*, vol. 10, no. 40, p. 2002341, Oct. 2020, doi: 10.1002/aenm.202002341.

[42] A. Zakutayev, "Brief review of emerging photovoltaic absorbers," *Current Opinion in Green and Sustainable Chemistry*, vol. 4. Elsevier B.V., pp. 8–15, Apr. 2017, doi: 10.1016/j.cogsc.2017.01.002.

[43] J. Yin and J. Jia, "Synthesis of Cu3BiS3 nanosheet films on TiO2 nanorod arrays by a solvothermal route and their photoelectrochemical characteristics," *CrystEngComm*, vol. 16, no. 13, pp. 2795–2801, Apr. 2014, doi: 10.1039/c3ce41958d.

[44] L. Whittaker-Brooks, J. Gao, A. K. Hailey, C. R. Thomas, N. Yao, and Y. L. Loo, "Bi2S3 nanowire networks as electron acceptor layers in solution-processed hybrid solar cells," *J. Mater. Chem. C*, vol. 3, no. 11, pp. 2686–2692, 2015, doi:

10.1039/c4tc02534b.

[45] S. Wang, X. Y. Liu, and Y. Z. Gu, "Excellent photoelectric properties and charge dynamics of two types of bulk heterojunction solar cells," *Mater. Lett.*, vol. 166, pp. 251–254, 2016, doi: 10.1016/j.matlet.2015.12.085.

[46] "Oxide Semiconductors for Solar Energy Conversion: Titanium Dioxide - Janusz Nowotny - Google Книги." https://books.google.ee/books?id=AlTVUs3IlEwC&pg=PA156&redir_esc=y#v=onepage&q&f=false (accessed Feb. 04, 2021).

[47] T. Ivanova, A. Harizanova, T. Koutzarova, and B. Vetruyen, "Electrochromic and optical study of sol-gel TiO2-MnO films," in *Journal of Physics: Conference Series*, Jun. 2020, vol. 1492, no. 1, p. 012028, doi: 10.1088/1742-6596/1492/1/012028.

[48] X. Yang, Q. Bi, H. Ali, K. Davis, W. V. Schoenfeld, and K. Weber, "High-Performance TiO_2 -Based Electron-Selective Contacts for Crystalline Silicon Solar Cells," *Adv. Mater.*, vol. 28, no. 28, pp. 5891–5897, Jul. 2016, doi: 10.1002/adma.201600926.

[49] X. Mei *et al.*, "Efficient CdTe Nanocrystal/TiO2 Hetero-Junction Solar Cells with Open Circuit Voltage Breaking 0.8 V by Incorporating A Thin Layer of CdS Nanocrystal," *Nanomaterials*, vol. 8, no. 8, p. 614, Aug. 2018, doi: 10.3390/nano8080614.

[50] V. V. Satale and S. V. Bhat, "Superstrate type CZTS solar cell with all solution processed functional layers at low temperature," *Sol. Energy*, vol. 208, pp. 220–226, Sep. 2020, doi: 10.1016/j.solener.2020.07.055.

[51] J. Ma *et al.*, "Enhanced Planar Perovskite Solar Cell Performance via Contact Passivation of "2/Perovskite Interface with NaCl Doping Approach," *ACS Appl. Energy Mater.*, vol. 1, no. 8, pp. 3826–3834, Aug. 2018, doi: 10.1021/acsaem.8b00602.

[52] V. C. Anitha, A. N. Banerjee, and S. W. Joo, "Recent developments in TiO2 as n- and p-type transparent semiconductors: synthesis, modification, properties, and energy-related applications," *Journal of Materials Science*, vol. 50, no. 23. Kluwer Academic Publishers, pp. 7495–7536, Dec. 29, 2015, doi: 10.1007/s10853-015-9303-7.

[53] E. Kärber, A. Katerski, I. Oja Acik, A. Mere, V. Mikli, and M. Krunks, "Sb2S3 grown by ultrasonic spray pyrolysis and its application in a hybrid solar cell," *Beilstein J. Nanotechnol.*, vol. 7, no. 1, pp. 1662–1673, Nov. 2016, doi: 10.3762/bjnano.7.158.

[54] R. Parize *et al.*, "ZnO/TiO2/Sb2S3 Core–Shell Nanowire Heterostructure for Extremely Thin Absorber Solar Cells," *J. Phys. Chem. C*, vol. 121, no. 18, pp. 9672–9680, 2017, doi: 10.1021/acs.jpcc.7b00178.

[55] H. S. Yun, B. wook Park, Y. C. Choi, J. Im, T. J. Shin, and S. Il Seok, "Efficient Nanostructured TiO2/SnS Heterojunction Solar Cells," *Adv. Energy Mater.*, vol. 9, no. 35, p. 1901343, Sep. 2019, doi: 10.1002/aenm.201901343.

[56] H. Huang *et al.*, "TiO2 surface oxygen vacancy passivation towards mitigated interfacial lattice distortion and efficient perovskite solar cell," *Appl. Surf. Sci.*, vol. 544, p. 148583, Apr. 2021, doi: 10.1016/j.apsusc.2020.148583.

[57] A. Graf *et al.*, "Electrical characterization of annealed chemical-bath-deposited CdS films and their application in superstrate configuration CdTe/CdS solar cells," *Thin Solid Films*, vol. 582, pp. 351–355, 2015, doi: 10.1016/j.tsf.2014.11.003.

[58] F. Scarpelli, T. F. Mastropietro, T. Poerio, and N. Godbert, "Mesoporous TiO2 Thin Films: State of the Art," in *Titanium Dioxide - Material for a Sustainable Environment*,

InTech, 2018.

[59] "ETIS - Development of Sb2Se3 thin film solar cells by close-spaced sublimation." https://etis.ee/Portal/Mentorships/Display/b230c9e4-f108-49c4-b980-af9de559c633?lang=ENG (accessed Apr. 24, 2021).

[60] R. Krautmann, "DEVELOPMENT OF Sb 2 Se 3 THIN FILM SOLAR CELLS BY CLOSE-SPACED SUBLIMATION," TALLINN UNIVERSITY OF TECHNOLOGY, 2019.

[61] S. Rahemi Ardekani, A. Sabour Rouh Aghdam, M. Nazari, A. Bayat, E. Yazdani, and E. Saievar-Iranizad, "A comprehensive review on ultrasonic spray pyrolysis technique: Mechanism, main parameters and applications in condensed matter," *Journal of Analytical and Applied Pyrolysis*, vol. 141. Elsevier B.V., p. 104631, Aug. 01, 2019, doi: 10.1016/j.jaap.2019.104631.

[62] M. F. García-Sánchez *et al.*, "Nanostructured YSZ thin films for solid oxide fuel cells deposited by ultrasonic spray pyrolysis," *Solid State Ionics*, 2008, doi: 10.1016/j.ssi.2008.01.088.

[63] Mohamed Samer, "Pyrolysis," 2017. https://books.google.ee/books?hl=ru&lr=&id=3HCPDwAAQBAJ&oi=fnd&pg=PA223&dq=USP+precursor+solution+and+initiates+their+rapid+vaporization+&ots=6qStr0VP70&sig=1rQ5nOyoUe9xWftbQvncNHgjxO0&redir_esc=y#v=onepage&q&f=false (accessed Feb. 11, 2021).

[64] J. K. Saha, R. N. Bukke, N. N. Mude, and J. Jang, "Significant improvement of spray pyrolyzed ZnO thin film by precursor optimization for high mobility thin film transistors," *Sci. Rep.*, vol. 10, no. 1, pp. 1–11, Dec. 2020, doi: 10.1038/s41598-020-65938-6.

[65] A. Nakaruk, D. Ragazzon, and C. C. Sorrell, "Anatase thin films by ultrasonic spray pyrolysis," *J. Anal. Appl. Pyrolysis*, vol. 88, no. 1, pp. 98–101, 2010, doi: 10.1016/j.jaap.2010.03.001.

[66] R. Suresh, V. Ponnuswamy, and R. Mariappan, "Effect of solvent and substrate temperature on morphology of cerium oxide thin films by simple nebuliser spray pyrolysis technique," *Mater. Technol.*, 2015, doi: 10.1179/1753555714Y.0000000183.

[67] "Methods for Assessing Surface Cleanliness," in *Developments in Surface Contamination and Cleaning, Volume 12*, Elsevier, 2019, pp. 23–105.

[68] "8.2.1 Qualitative Analysis - Knovel." https://app.knovel.com/web/view/khtml/show.v/rcid:kpHATCST01/cid:kt0052L1C7/viewerType:khtml/root_slug:8-x-ray-diffraction/url_slug:x-ray-diffraction?kpromoter=federation&b-toc-cid=kpHATCST01&b-toc-root-slug=&b-toc-url-slug=x-ray-diffraction&b-toc-title=Handbook of Analytical Techniques in Concrete Science and Technology&page=2&view=collapsed&zoom=1 (accessed Feb. 10, 2021).

[69] "Crystallography. Scattering and diffraction. The Bragg's Law." https://www.xtal.iqfr.csic.es/Cristalografia/parte_05_5-en.html (accessed Feb. 10, 2021).

[70] "UV Vis Spectroscopy | UV Vis Spectroscopy Applications | Edinburgh Instruments." https://www.edinst.com/techniques/uv-vis-spectroscopy (accessed May 04, 2021).

[71] M. Üürike, "INFLUENCE OF pH ON THE PROPERTIES OF CHEMICALLY DEPOSITED CdS

THIN FILMS AND SOLAR CELLS," Tallinn University of Technology, 2017.

[72] Y. Yan, "Tribology and tribo-corrosion testing and analysis of metallic biomaterials," *Met. Biomed. Devices*, pp. 178–201, 2010, doi: 10.1533/9781845699246.2.178.

[73] "Scanning Electron Microscopy - Nanoscience Instruments." https://www.nanoscience.com/techniques/scanning-electron-microscopy/ (accessed Feb. 10, 2021).

[74] A. Ul-Hamid and A. Ul-Hamid, "Imaging with the SEM," in *A Beginners' Guide to Scanning Electron Microscopy*, Springer International Publishing, 2018, pp. 129–180.

[75] D. R. Baer and S. Thevuthasan, "Characterization of Thin Films and Coatings," in *Handbook of Deposition Technologies for Films and Coatings*, Elsevier Inc., 2010, pp. 749–864.

[76] J. Moulder, W. Stickle, P. Sobol, and K. Bomben, "Handbook of X-ray Photoelectron Spectroscopy Perkin-Elmer Corp., Physical Electronics Division, Eden Prairie, Minnesota, USA, 1979.," *Surf. Interface Anal.*, 1981.

[77] "X-Ray Photoelectron Spectroscopy (XPS) Surface Analysis Technique." https://www.phi.com/surface-analysis-techniques/xps-esca.html (accessed May 06, 2021).

[78] R. R. Mather, "Surface modification of textiles by plasma treatments," in *Surface Modification of Textiles*, Elsevier Inc., 2009, pp. 296–317.

[79] P. Würfel, "Physics of Solar Cells: From Principles to New Concepts," *Physics of Solar Cells: From Principles to New Concepts*. pp. 1–186, 2007, doi: 10.1002/9783527618545.

[80] "(PDF) Functional graphene: synthesis, characterization and application in optoelectronics." https://www.researchgate.net/publication/283662836_Functional_graphene_synthesis_characterization_and_application_in_optoelectronics (accessed May 06, 2021).

[81] "Quantum Efficiency | PVEducation." https://www.pveducation.org/pvcdrom/solar-cell-operation/quantum-efficiency (accessed Apr. 19, 2021).

[82] G. B. Harris, "X. Quantitative measurement of preferred orientation in rolled uranium bars," *London, Edinburgh, Dublin Philos. Mag. J. Sci.*, vol. 43, no. 336, pp. 113–123, 1952, doi: 10.1080/14786440108520972.

[83] X. Pan, M. Q. Yang, X. Fu, N. Zhang, and Y. J. Xu, "Defective TiO2 with oxygen vacancies: Synthesis, properties and photocatalytic applications," *Nanoscale*, vol. 5, no. 9. The Royal Society of Chemistry, pp. 3601–3614, May 07, 2013, doi: 10.1039/c3nr00476g.

[84] N. Spalatu *et al.*, "Effect of CdCl2annealing treatment on structural and optoelectronic properties of close spaced sublimation CdTe/CdS thin film solar cells vs deposition conditions," *Thin Solid Films*, vol. 582, pp. 128–133, 2015, doi: 10.1016/j.tsf.2014.11.066.

[85] N. Spalatu, M. Krunks, and J. Hiie, "Structural and optoelectronic properties of CdCl2 activated CdTe thin films modified by multiple thermal annealing," *Thin Solid Films*, vol. 633, pp. 106–111, 2017, doi: 10.1016/j.tsf.2016.09.042.

[86] I. Dundar, M. Krichevskaya, A. Katerski, and I. O. Acik, "TiO 2 thin films by ultrasonic

spray pyrolysis as photocatalytic material for air purification," *R. Soc. Open Sci.*, vol. 6, no. 2, 2019, doi: 10.1098/rsos.181578.

[87] I. Dundar, M. Krichevskaya, A. Katerski, M. Krunks, and I. O. Acik, "Photocatalytic degradation of different VOCs in the gas-phase over TiO2 thin films prepared by ultrasonic spray pyrolysis," *Catalysts*, vol. 9, no. 11, p. 915, Nov. 2019, doi: 10.3390/catal9110915.